ACS OMEGA

Open Access

http://pubs.acs.org/journal/acsodf

Article

Isolation, Characterization, and Single-Crystal X-ray Analysis of Lantabetulic Acid from *Rhus alata*: Insights into HSA and BSA Binding Interactions, with In-Silico Study

Mehtab Parveen,* Uzma, Azmat Ali Khan, Shahab A. A. Nami, Ramesh Kataria, Abdul Malik, Nurul Afiqah Muhammad Amali, Nurul Huda Abd Kadir,* and Mahboob Alam*

Cite This: *ACS Omega* 2024, 9, 39484−39502

Read Online

ACCESS | Metrics & More | Article Recommendations | Supporting Information

ABSTRACT: This study investigated the bioactive potential of *Rhus alata*, a plant known for its rich phytochemicals. A previously unreported compound was isolated from *R. alata* and characterized using various spectroscopic techniques (IR, UV, NMR, MS) and confirmed for the first time by X-ray crystallography. In isolated compound 1, noncovalent interactions between H···H/H···H, C···C/C···C and O···H/H···O play a major role in its packing arrangement. This observation is consistent with the results of Hirshfeld surface analysis, which quantified these interactions as 14.2%, 84.6%, and 1.2%, respectively. The isolated compound was identified as lantabetulic acid (**1**) (3*β*,25-expoxy-3*α*-hydroxylup-20(29)-en-28-oic acid). To understand its potential biological interactions, the binding affinity of lantabetulic acid to biomolecules such as bovine serum albumin (BSA), and human serum albumin (HSA), was assessed. The results showed significant binding efficacy, indicating potential interactions with these molecules. Furthermore, the DPPH assay demonstrated the potent antioxidant activity of this compound. We used in silico molecular docking to clarify the binding affinity between lantabetulic acid and a particular receptor. Furthermore, molecular dynamic simulation studies also explored the binding interaction. As well, MM/GBSA calculations corroborate the simulation results and the stability of the complex. Docking and dynamics studies revealed promising binding scores, suggesting further investigation into their potential therapeutic applications. Geometric parameters and the absorption spectrum of compound 1 were also determined using the DFT approach and compared with experimental findings.

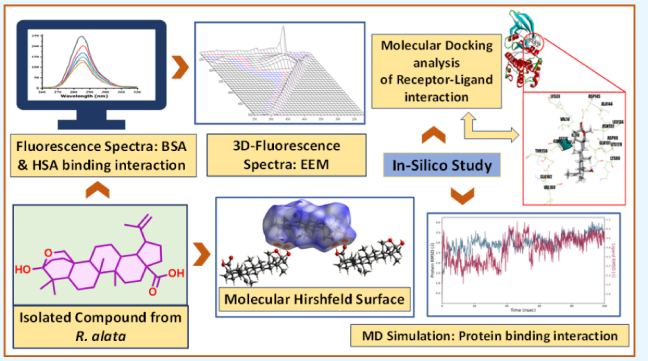

1. INTRODUCTION

Since ancient times, natural resources have been a source of therapeutic agents. It is impossible to exaggerate the value of plants in treating human illnesses.[1] An endless supply of bioactive chemicals in the plant kingdom is priceless in treating numerous incurable diseases.[2] Medicinal plants typically exhibit complex pharmacological responses due to multiple active components.[3] These active metabolites that the plants produce have a broad range of medicinal uses, including skin treatment, antiviral, anticancer, antidiabetic, antifungal, and antimicrobial properties. The multidisciplinary approach of isolating a drug molecule using plants and biogenies has gained a lot of attraction in the drug discovery process.[4] Medicinal plants contain certain bioactive compounds that have been demonstrated to inhibit cancer cell growth and promote apoptosis, a process that naturally destroys cancer cells. Furthermore, these bioactive chemicals may have the ability to disrupt different cellular processes involved in cancer growth and progression.[5] Scientists have turned their focus to the isolation and characterization of bioactive molecules in recent years due to several advantages, most notably that it has relatively few side effects compared to traditional allopathic medications.[6]

Albumin, the most prevalent kind of protein in serum, has a major impact in cell physiological well-being.[7] Albumin maintains blood oncotic pressure and pH, binds and transports essential ligands, and acts as an antioxidant. It interacts with cells in animal tissues and cultured cells, influencing circulation, as well as research and commercial applications.[8]

R. alata, often known as "African Sumac" or "African Waxberry," belongs to the plant family Anacardiaceae.[9] The Anacardiaceae family contains 73 genera and over 600 species. The largest (approximately 60 species) genus of climbers, Shrubs, and trees. Rhus usually occurs in the warm temperate

Received: April 9, 2024
Revised: September 1, 2024
Accepted: September 4, 2024
Published: September 12, 2024

zones of both hemispheres, with some distribution into the tropical and lower temperate zones. Since ancient times, the *Rhus alata* plant has been used for its medicinal benefits.[9,10] Numerous Indian species are used extensively in traditional medicine as anticancer, antioxidant,[11] antiviral, antibacterial,[12] and spasmolytic agents. Some species may induce dermatitis in sensitive individuals. Antioxidant-rich compounds are present in *Rhus alata* extracts. These compounds, including flavonoids and phenolic compounds, may aid in scavenging free radicals and lowering oxidative stress in cells.[13] Antioxidants benefit general health since they can aid in preventing chronic diseases.[9]

Since there are limited studies on the medicinal potential of *R. alata* leaves, we performed a comprehensive analysis since biflavonoids, triterpenes, and benzofuranoic acids were previously identified in these plant leaves.[14] This study reports the isolation and characterization of a new compound named lantabetulic acid (**1**) from *R. alata*, despite its previously reported presence in a sister species. Additionally, five previously known compounds were identified from *R. alata* leaves, namely ethyl gallate, suberin, dimethyl terephthalate, oleanolic acid, and lupeol. The isolated compounds' structures were characterized by means of spectroscopic techniques including FTIR, UV, ^{1}H and ^{13}C NMR, and MS. The structure of the isolated compound (1) was also confirmed using X-ray crystallography and appeared as white crystals after crystallization.

The goal of our current research focuses on isolating and characterizing bioactive compounds using physicochemical tools. Single-crystal X-ray diffraction was then employed to definitively confirm the structure of the isolated compound. Additionally, this research aims to improve the efficacy, pharmacological properties, and accessibility of drugs. In this context, the interaction of lantabetulic acid (1) with biomolecules relevant to drug delivery and therapeutic effects was studied. These include bovine serum albumin (BSA), and human serum albumin (HSA). The binding affinity of lantabetulic acid (1) to these proteins was studied because this interaction can influence intracellular drug distribution and potentially modulate cell growth or death. To further elucidate the potential therapeutic role of lantabetulic acid (1), a DPPH assay was performed to evaluate its antioxidant properties. Additionally, molecular docking simulations were employed to gain a deeper understanding of the interactions between lantabetulic acid (1) and these biomolecules.

2. MATERIALS AND METHODS

2.1. General Experimental Procedure. Melting points are measured without correction using a Kofler apparatus. Elemental analysis (C, H, and N) has been performed using Thermo Scientific (FLASH 2000) CHN Elemental Analyzer. The PerkinElmer (2000 FTIR) Spectrometer used the KBr pellet method to collect Fourier transform-infrared (FT-IR) spectra. The recorded values are expressed in centimeters. A PerkinElmer UV Win Lab spectrophotometer was used to record the UV spectra. $CDCl_3$ solvent was utilized to record ^{1}H NMR and ^{13}C NMR spectra using Bruker Avance-II 400 and 100 MHz instruments. J values are expressed in Hertz, while chemical shifts (δ) are expressed in parts per million relatives to the TMS, which acts as an internal standard. A JEOLD-300 mass spectrometer was used to record the mass spectra. To verify the purity of collected compounds and fractions, silica gel G254 (E-Merck) was coated on glass plates used in thin-layer chromatography (TLC) and exposed to the fumes of iodine. The plates measured 20 × 5 and 50 × 10.

2.2. Plant Materials. The leaves of *R. alata* were procured from Pucchunga University College, Aizawl, Mizoram. It was identified by Professor Wazahat Hussain of the Department of Botany at A. M. U. in Aligarh, India.

2.3. Extraction and Isolation. Leaves of *R. alata* (Family: Anacardiaceae) (2 kg) were dried under shade and crushed to make powder. The air-dried powdered leaves were extracted under reflux with 95% ethanol and the solvent was removed by steam-distillation, a dark green gummy mass was obtained and fractionated with various solvents using petroleum ether (60−80 °C), benzene, ethyl acetate, acetone, and methanol). Petrol and benzene fractions showed similar behavior during the TLC examination and, hence, were mixed. The mix of petrol and benzene extract was separated by chromatography over a silica gel column.[11] It was eluted with petrol, petrol-benzene (9:1−1:1). The fraction obtained from petrol−benzene from 9:1 to 7:3 furnished various fractions which were crystallized into pure compounds and were identified as ethyl gallate, friedelin, dimethyl ester of terephthalic acid, oleanolic acid, and lupeol which were reported earlier.[15] Eluviation of column petrol-benzene (1:1) and benzene furnished various fractions that behave similarly on TLC and Co-TLC examination in various solvent systems (petrol-benzene 7:3, chloroform-benzene 9:1, benzene-ethyacetate9:1 and 8:2) and hence were pooled together. The mixed fraction was crystallized with chloroform-acetone into a crystalline solid marked as **1** (yield 25 mg, mp 249−250 °C).

2.4. Spectral Analysis of Isolated Compound: Lantabetulic Acid [IUPAC: 9-Hydroxy-5a,5b,8,8-tetramethyl-1-(prop-1-en-2-yl) octadecahydro-9,11a- (epoxymethano) cyclopenta[a] chrysene-3a(4H)-carboxylic acid (1)]. Compound **1** was crystallized from chloroform-acetone as white crystals (25 mg), m.p., 249−250 °C, Anal. Calc. for $C_{30}H_{46}O_4$; C, 76.68; H, 9.62; O, 13.52%; found: C, 76.55; H, 9.85; O, 13.52%. IR (KBr) ν cm^{-1}: 3420, 3000, 2852, 1723, 1680, 1464, 1375, 1029 cm^{-1}. ^{1}H NMR (400 MHz, $CDCl_3$, ppm) δ: 5.3 (s, 1H), 2.5 (s, 2H, -OCH_2), 4.4 and 4.6 (s, 2H, terminal CH_2). ^{13}C NMR (100 MHz, $CDCl_3$, ppm) δ:181, 154.95, 114.3, 101.7, 60.0, 43.5, 39.4, 26.4, 23.9, 18.7; MS (ESI) m/z: 453[$M^{+\bullet}$, 17]. The NMR spectra, mass spectrum, and UV−vis spectrum of the isolated compounds are given in Figures S1−S4.

2.5. Crystallographic Analysis. For X-ray diffraction of compound **1** single crystals at room temperature, A Bruker Kappa APEXII CCD X-ray diffractometer was utilized to measure the monochromatic wavelength of 0.71073 Å graphite-based Mo−K radiation. Adjustments for absorption were made using SADABS.[16] Using the direct method of SHELXL[17] and its complete matrix least-squares on F2, the predicted chemical structure of compound **1**. and isotopically refined (non-H atoms) was determined. Using isotropic displacement parameters, the hydrogen atoms in the structures were refined and placed in a superior position. The crystal structure was solved using a suite of software programs: CrystalClear-SM Expert 2.0 r7 (Rigaku, 2011)[18] for data processing, SHELXT 2014/5 (Sheldrick, 2014)[19] for structure solution, SHELXL 2018/3 (Sheldrick, 2015)[17] for refinement, Olex2 (Dolomanov et al., 2009)[20] for structure visualization, and Mercury for graphical representation. Table S1. explains the experiment setup required for the monocrystalline X-ray analysis of compound **1.** Crystal Explorer 17.5 software[21] was

https://doi.org/10.1021/acsomega.4c03406
ACS Omega 2024, 9, 39484−39502

employed to analyze the topological features of component 1 in the study.

2.6. Antioxidant Analysis. The free radical scavenging activity of ethanol extracts of *R. alata* leaves was evaluated using a DPPH (2,2-diphenyl-1-trinitrophenylhydrazine) assay. The activity of these extracts was then compared to that of ascorbic acid, a well-known antioxidant standard.[22] The whole procedure was determined according to the well-known methods of Braca.[23] Three ml of 0.4 mM DPPH solution which was kept for approximately 60 min in the dark under a cooling environment were combined with one ml of ascorbic acid solution (as a reference) at various concentrations (12.5, 25, 50, 100, and 200 μg/mL) and one ml of *R. alata* leaves extract solution at different concentrations (12.5, 25, 50, 100, and 200 μg/mL). The absorbance at 517 nm was measured with a UV−visible spectrophotometer, with ascorbic acid that serve as a positive control. A reduced absorbance of the reaction mixture suggested a greater tendency to scavenge free radicals. Extract scavenging efficiency was indicated by the degree of DPPH decolorization from purple to yellow. The following formula was used to determine the scavenging activity against DPPH:

$$\text{DPPH radicals scavenging activity I}(\%) = \left(\frac{\text{A blank} - \text{A standard}}{\text{A blank}}\right) \times 100$$

where, A standard = Absorbance of DPPH radical (without the test sample).

A blank = Absorbance of DPPH radical with the different extract samples of various concentrations.

The percentage of inhibition or scavenging activity was then plotted against the log concentration, and linear regression analysis was used to determine the IC50 (Inhibition concentration 50) value from the graph.[24] The 50 inhibitory concentration (IC50) was computed and expressed in μg/mL based on the RSA%. The minimum extract concentration to neutralize half of the initial stable free radical in 30 min in 1 mL of reaction in the dark is known as the IC50. To find the sample concentration needed to inhibit 50% of the radicals, the IC50 value was calculated. Samples exhibit increased antioxidant activity as the IC50 value decreases. According to antioxidant study Table 4. compound **1** had the highest antioxidant activity (13.772 μg/mL) based on the observed IC50 value, followed by reference ascorbic acid. Remarkably, the IC50 value of compound 1 was lower than that of ascorbic acid (18.312 μg/mL).

2.7. Molecular Docking, Molecular Dynamics (MD) Simulations, and Computational Details. Molecular docking of an isolated compound from *Rhus alata* with the crystal structure of the human cyclin-dependent kinase 2 (CDK2) complex. The CDK2 (PDB ID: 1hck) complex was obtained from the Protein Data Bank. The geometry coordinates derived from the CIF file were subsequently employed to design a chemical structure for molecular docking investigation. Before docking, the chemical structure was energy minimized using the MM2 force field and saved in PDB format. The PDB structure (PDB ID: 1hck) was then downloaded and prepared for docking. This involves adding polar hydrogens to the protein and removing any cocrystallized heterocyclic compounds or water molecules from its active site. Active sites are identified by analyzing cocrystallized molecules. Subsequently, the web server Webina is used to define the docking grid center based on the identified active site locations. Docking simulations were performed using Vina software integrated in Webina.[25] The docking pose with the highest score was selected and further analyzed for non-covalent interactions between the receptor (CDK2) and the ligand (compound **1**) using BIOVIA Discovery Studio Visualizer. This analysis provides valuable insights into the mechanisms of interactions between compounds. and protein. Molecular dynamics (MD) simulations were performed using Schrödinger-Desmond software to investigate the dynamics and interactions of the ligand-protein complex.[26] The system was modeled using the OPLSA force field. The complex was dissolved in a 10 Å orthogonal box using the TIP3P water model and then neutralized with chloride ions. The two phases were equilibrated at a temperature and pressure of 300 K and 1 bar, respectively. Afterward, the MD simulations were run for 100 ns. To understand the behavior of the complex, the trajectory data of the MD simulations were examined. The root-mean-square fluctuation (RMSF) and root-mean-square deviation (RMSD) were calculated to assess the overall and per-residue mobility of the protein. The ligand torsion angles and hydrogen bonding patterns were also examined. The complex analysis results were visualized using Schrödinger-Desmond software. The Prime module of Maestro employed the MM/GBSA (molecular mechanics/generalized Born surface area) method to calculate the binding free energy of the ligand-protein complex. For these calculations, variational solvation with the generalized Born model (VSGB) model and the OPLS3e force field was used. Density Functional Theory (DFT) calculations on the isolated compound lantabetulic acid (1) were performed using the B3LYP functional,[27] which combines Becke's three-parameter exchange functional with the Lee−Yang−Parr correlation functional, in combination with the 6−311++G(d,p) basis set.[28] Solvent effects were incorporated using the Polarizable Continuum Model (PCM),[29] a commonly used implicit solvent method, with a dielectric constant of 4.81 for chloroform. All calculations were carried out with the Gaussian 09 software package[30] to compare geometric parameters and the absorption spectrum with experimental data for compound **1**.

2.8. Preparation of HSA Solution and Fluorescence Measurement of Lantabetulic Acid (1) Binding to HSA. The interactions of HSA and BSA with the isolated compound were investigated using a slight modification of the previously described procedure.[31] One μM HSA solution was prepared by dissolving 66.394 mg of HSA with phosphate saline buffer. Then, 50 μL of HSA was pipetted into a 96-well plate with 50 μL treatment. The plate then was read by using a microplate reader. After that, the temperature was set for 300 and 310 K of microplate reader with wavelength 300 nm (start) − 530 nm (stop). Lastly, the data obtained were recorded to plot the graph. A step-by-step approach for the binding interaction between compound 1 under study and human serum albumin (HSA) is shown in Figure 2. The exact concentration of HSA and BSA in the samples was estimated spectrophotometrically at 280 nm using their individual molar extinction coefficients (36,500 M^{-1} cm^{-1} for HSA and 43 824 M^{-1} cm^{-1} for BSA) based on the Beer−Lambert Law.

2.9. Preparation of BSA Solution and Fluorescence Measurement of Lantabetulic Acid (1) Binding to BSA. Prepare a 1 μM BSA solution by dissolving 66.394 mg BSA in PBS (4950 μL PBS + 50 μL BSA). Then, 50 μL of BSA was pipetted into a 96-well plate containing 50 μL of treatment

https://doi.org/10.1021/acsomega.4c03406
ACS Omega 2024, 9, 39484−39502

solution. The plate is then read using a microplate reader. Afterward, the temperature of the microplate reader was set to 300 and 310 K, and the wavelength was 300 nm (start) and 530 nm (stop). Finally, the graph was plotted using the data that was collected.

3. RESULT AND DISCUSSION

3.1. Structural Elucidation. The 2 kg of dried *R. alata* leaves were extracted with 95% ethanol under reflux, and the solvent was removed via steam-distillation, a dark green gummy mass was obtained and fractionated with various solvents using petroleum ether (60−80 °C), benzene, ethyl acetate, acetone, and methanol). Since petrol and benzene extract showed similar behavior on TLC examination and followed a positive response on the terpenoidic test and were mixed and chromatographed over a silica gel column. Elution of the columns with petrol and petrol-benzene (9:1−7:3) gave various fractions which upon crystallization gave previously reported compounds ethyl gallate, friedelin, dimethyl ester of terephthalic acid, oleanolic acid, and lupeol.[15] The compound (**1**) was obtained from petrol-benzene (1:1). Eluate upon crystallization with chloroform and acetone afforded with shinning crystal (yield 25 mg, mp 249−250 °C).[32] Based on the above assignment, the compound was identified as lantabetulic acid (**1**) (Figure 1), a new compound not previously reported in particular plants; however, compound 1 has been reported from sister species of this plant (Figure 2).

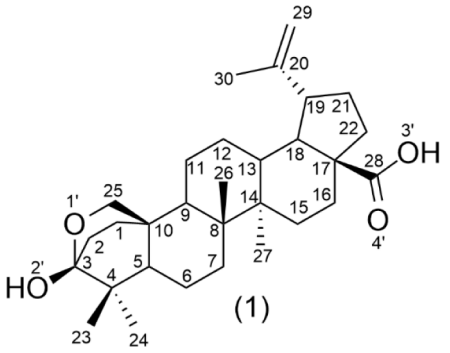

Figure 1. Chemical structure of the isolated lantabetulic acid (1) and its numbering according to the nomenclature mentioned in IUPAC.

Lantabetulic acid (**1**) was isolated as white crystals and molecular formula $C_{30}H_{46}O_4$ was determined by analysis of its ESI-MS spectrum m/z 453 $[M^{+\bullet}]$ calculated for $C_{30}H_{46}O_4$. Elemental analysis confirmed the proposed molecular formula $C_{30}H_{46}O_4$. In the ultraviolet spectrum, the compound (**1**) showed distinct absorption bands at 210 and 293 nm, showing an acidic and strong hydroxyl group in the skeleton. Its IR spectrum revealed absorption bands at 3420, 3000, 2852, 1680, and 1464 cm^{-1}, revealing the existence of a hydroxyl group (OH), C−H stretching, C = C, carbonyl group (C = O) functional groups in the molecule (Figure 3). The ^{1}H NMR spectra showed a distinct, sharp singlet peak for a single proton at δ 5.3 ascribed to a hydroxylic OH proton. In contrast, a coupled pair of singlets at δ 4.4 and 4.6 for 2H (terminal CH_2). Another peak at δ 2.5 for 2H at bridging O−CH_2 and a singlet peak was demonstrated at δ 11.0 for carboxylic acid OH. The ^{13}C NMR spectrum signals at δ 181, 154.95, 114.3, 101.7, 60.0, 43.5, 39.4, 26.4, 23.9, and 18.7 have also supported the assigned structure of the compound.

The UV−visible spectrum of compound 1 in chloroform (Figure 4) showed a prominent peak at 216 nm, consistent with the presence of a π-electron system of 2-methylpropene associated with the cyclopentane ring. Furthermore, the moderate intensity peaks at 264 and 286 nm may be attributed to electronic transitions within the epoxide and/or carboxylic acid functional groups, although the electronic influence of neighboring groups could not be ignored.

The electronic absorption spectrum was also calculated using Time-Dependent Density Functional Theory (TD-DFT) at the B3LYP/6-311++G(d,p) level of theory to compare the experimental data with the simulated UV−vis data. The structure of the molecule was optimized in the gas phase using the same basis set. To account for solvent effects, the electronic spectra in chloroform ($CHCl_3$) were simulated using the Polarizable Continuum Model (PCM). The calculated excitation energies, wavelengths, oscillator strengths, and dominant HOMO−LUMO contributions are presented in PC13Table 1. Figure 4 presents a comparison of the theoretical and experimental UV/vis spectra, illustrating a strong correlation between the two. The spectrum of the isolated compound in $CHCl_3$ solution showed a prominent peak at 216 nm and two smaller peaks at 264 and 284 nm. The spectrum calculation indicated peaks in the range of 208 to 216 nm in solution, with contributions from HOMO−LUMO interactions ranging from 75% to 4%. Additionally, some smaller peaks resulting from other HOMO−LUMO interactions were observed (Table 1).

Additional single-crystal X-ray crystallography analysis verified the compound's molecular makeup 1. It is a new compound, and the data as mentioned above led to the conclusion that compound is lantabetulic acid (1) (or 3β,25-expoxy-3α-hydroxylup-20(29)-en-28-oic acid or 9-hydroxy-5a,5b,8,8-tetramethyl-1-(prop-1-en-2-yl) octadecahydro-9,11a-(epoxymethano) cyclopenta[a] chrysene-3a(4H)-carboxylic acid). The supplementary data in Figures S1−S3 provides the NMR spectra, and mass spectrum of the isolated compound 1.

3.2. Crystal Structure Description. Figure 1 shows the molecular structure of compound **1** (Figures 1, 5 and 6), obtained by single-crystal X-ray diffraction analysis. Table 2 lists some of the selected bond angles and bond distances of the isolated compound. The Orthorhombic system was observed in the crystallized compound and a noncentrosymmetric $P2_12_12_1$ space group, with lattice parameters a = 7.1010 (7) Å, b = 19.0735 (19) Å, c = 19.172 (2) Å along with cell anglers α = 90, β = 90, γ = 90o. The asymmetric unit contained one molecule, while the unit cell comprised four molecules. The crystal density was 1.204 g/cm^3 and the unit cell volume was 2596.7(5) Å3. Multiple ring systems are present in the molecule, including cyclopentane rings. The six-membered ring of the compound **1** scaffold assumes a chair conformation. The cyclopentane ring exhibits a twisted envelope structure. The orientation of the propene group concerning the five-membered ring in compound **1** is defined by the dihedral angle formed by C6, C30, C24, and C2. The measurement of this angle is 179.17 degrees. The C = C bond length between C2 and C30 shows a value of 1.315 Å, confirming its double bond character. In addition, the bond lengths of the hydroxyl group at C18 and the carboxylic acid group attached to C28 are 1.401 and 1.328 Å, respectively (Table 2). Our measured bond lengths are in good agreement with the values reported in the literature. Individual molecules interact with each other

https://doi.org/10.1021/acsomega.4c03406
ACS Omega 2024, 9, 39484−39502

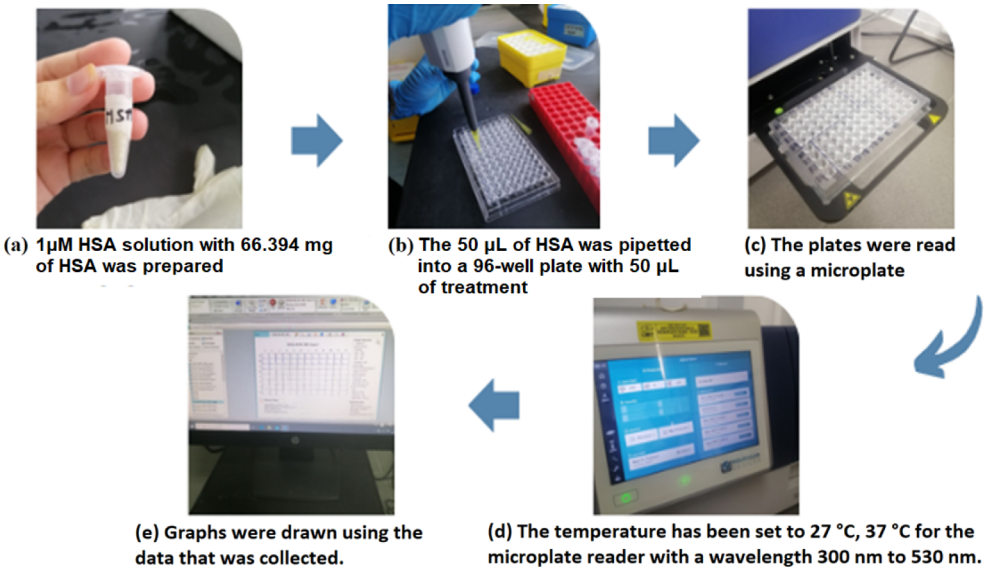

Figure 2. Step-by-step procedure to prepare HSA (or BSA) solution and reading fluorescence of compound 1 with HSA.

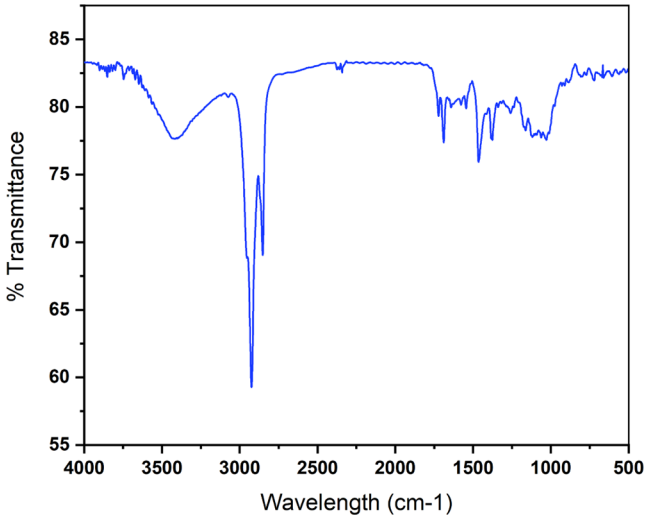

Figure 3. FTIR spectrum of compound **1**.

through weak C−H---O hydrogen bonds. These bonds involve specific oxygen and hydrogen atoms (O19···H19−O29 and O24−H24---O30), the details of which are shown in Table 2. One of the oxygen atoms involved in this hydrogen bonding is part of an epoxymethano functional group. Figure 6 and Table 3 illustrate all of the intermolecular C−H---O interactions that affect how molecules pack together. DFT/B3LYP/6-311++G(d,p) calculations of the isolated compound were performed to compare geometric parameters. The Gaussian 09 software facilitated these calculations, providing insights into the geometric parameters and absorption spectrum, which were subsequently compared with experimental data to validate the computational model (Figure 4). The gas-phase molecule yielded geometric parameters that exhibit good agreement with the experimental solid-state data. However, as anticipated, due to the differing environments, some deviations are present. Notably, Table 2 shows these discrepancies, particularly for C−H and O−H bonds. The calculated bond lengths (1.084 and 0.964 Å, respectively) deviate slightly from the experimental values (0.930 and 0.820 Å, respectively). A recurring trend is observed where C−H, N−H, O−H, and C−S bond lengths exhibit larger deviations compared to other parameters.[33] These discrepancies might arise not only from the limitations of the gas-phase model but also from the basis set used or neglecting vibrational effects. Our calculations revealed bond angles of 107.3°, 106.5°, 120.8°, and 118° for C18−O24−H24, C28−O29−H29, O30−C28−O29, and H2A−C2-H2B, respectively. These values show a good correlation with experimental data. However, slight deviations are observed due to the difference between the gas-phase model used in the calculations and the actual molecule's solid-state environment. Experimental bond angles were found to be 110.95°, 109.5°, 122.2°, and 120°, respectively, further supporting the overall agreement with the experiment. For compound **1**, the experimental dihedral angles were 169.49° for the methyl carbon (C24) of propene, 106.3° for the unsaturated carbon (C2) of propene, and 105.9° for the carbon atoms (C5 and C7) of the cyclopentane ring. These values differ slightly from the dihedral angles obtained by DFT calculations (169.0° and 96.6°, respectively). The difference in phases between the experiment (solid state) and the DFT calculation (gaseous phase) also accounts for these discrepancies.

3.3. Hirshfeld Surface. The extraordinary method described involves exploring packing patterns and intermolecular interactions in molecular crystals through the use of molecular Hirshfeld surfaces. These surfaces provide a unique visual representation of intermolecular interactions in a crystalline environment, providing insights into the shape of molecules. In this method, it summarizes the interactions between molecules in a substance by generating a two-dimensional diagram. The diagram identifies several types of interactions, such as hydrogen bonds and van der Waals forces, using the distance between adjacent atoms. This allows researchers to easily group and compare crystal structures based on how the molecules interact. The 3D surface shading methods discussed involve assigning different colors to indicate various normal vector values on the surface. In this scheme, red represents negative d_{norm} values associated with close contact, blue represents positive values representing longer interactions,[34] and white represents a d_{norm} value of zero as shown in Figure 7. Hirshfeld surface analysis (Figure 7a) reveals

https://doi.org/10.1021/acsomega.4c03406
ACS Omega 2024, 9, 39484−39502

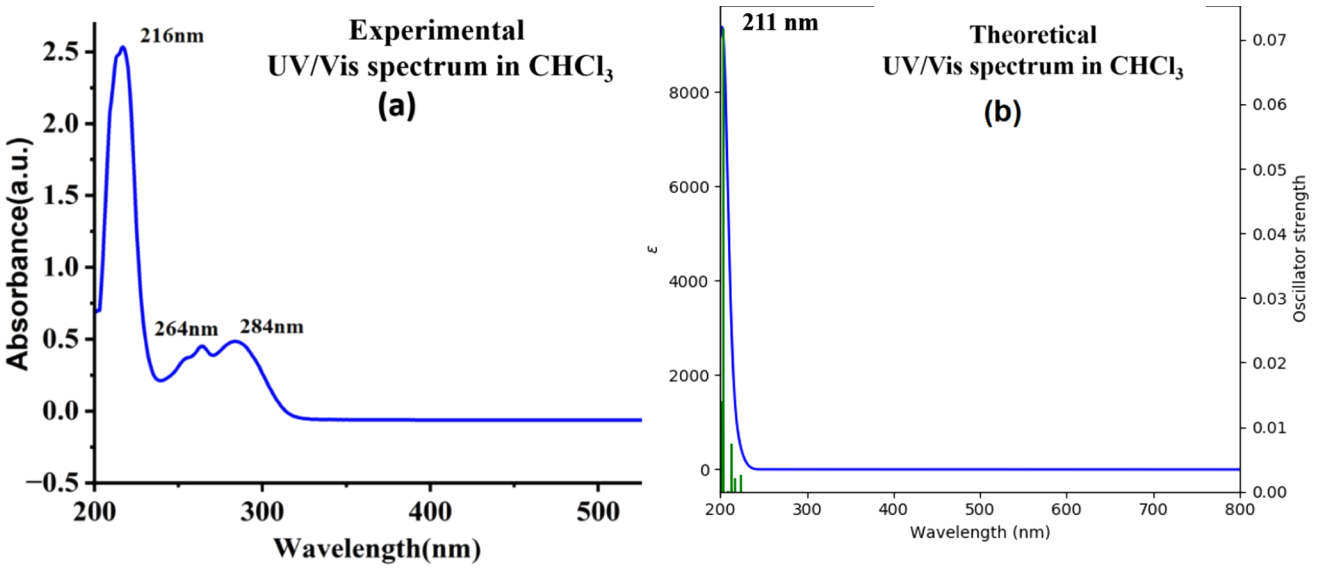

Figure 4. Comparison of (a) experimentally measured and (b) computationally predicted UV/vis spectra.

Table 1. Theoretical vs. Experimental UV/Vis Data of the Isolated Compound in $CHCl_3$a[a]

	PCM-TD-B3LYP/6-311++G(d,p)			
λ_{obs} (nm) in $CHCl_3$	λ_{calc} (nm)	E (eV)	f	Major and minor contributions (in%)
216	208	5.94	0.0001	H-1→L(16%); H→L(75%); H-1→L+1 (43%); H-1-
264	211	5.82	0.0075	>L+3. (18%); H→L+2. (17%); H-1→L+5 (5%),H-
284	216	5.71	0.002	>L+1 (4%); H→L+3(6%); H-1→L(72%); H-
	204	6.07	0.071	L(17%); H-1→L+4 (50%),H→L+4 (17%); H-1-
	203	6.08	0.0098	>L+4 (13%); H→L+1 (13%); H→L+3 (28%); H→L+5 (15%)

[a]H-HOMO, L-LUMO, E-excitation energy, f-oscillator strength.

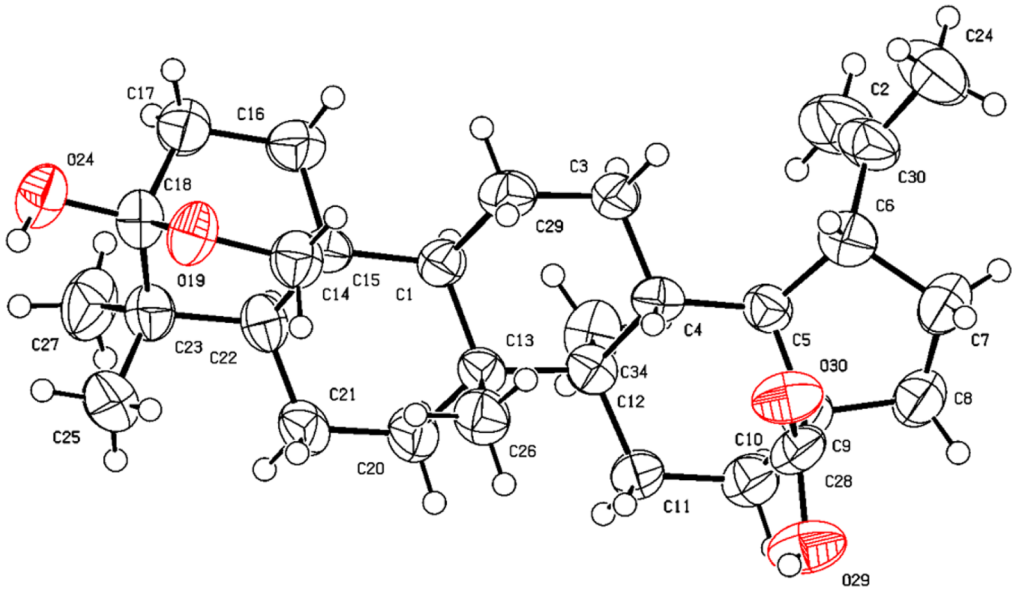

Figure 5. ORTEP diagram of 3β,25-epoxy-3β-hydroxylup-20(29)-en-28-oic acid (**1**). The atomic numbering scheme follows the diffraction pattern and is displayed at a 50% probability level.

prominent red regions concentrated around the oxygen atoms O19, O24, O29, and O30. These regions correspond to epoxymethane, hydroxyl, and carboxylic acid functional groups, indicating intermolecular interactions that control crystal packing. Furthermore, the fingerprints (Figure 7b,c) depict these long-range interactions through the presence of blue regions. The fingerprint (Figure 7c) shows two elongated spikes indicating long-range interactions, corresponding to hydrogen bonds that contribute 14.2% interatomic contacts to the Hirshfield surface. The major contribution to the total Hirshfield surface area comes from H···H/H···H interactions, accounting for 84.6%. Although they are ubiquitous on the

https://doi.org/10.1021/acsomega.4c03406
ACS Omega 2024, 9, 39484−39502

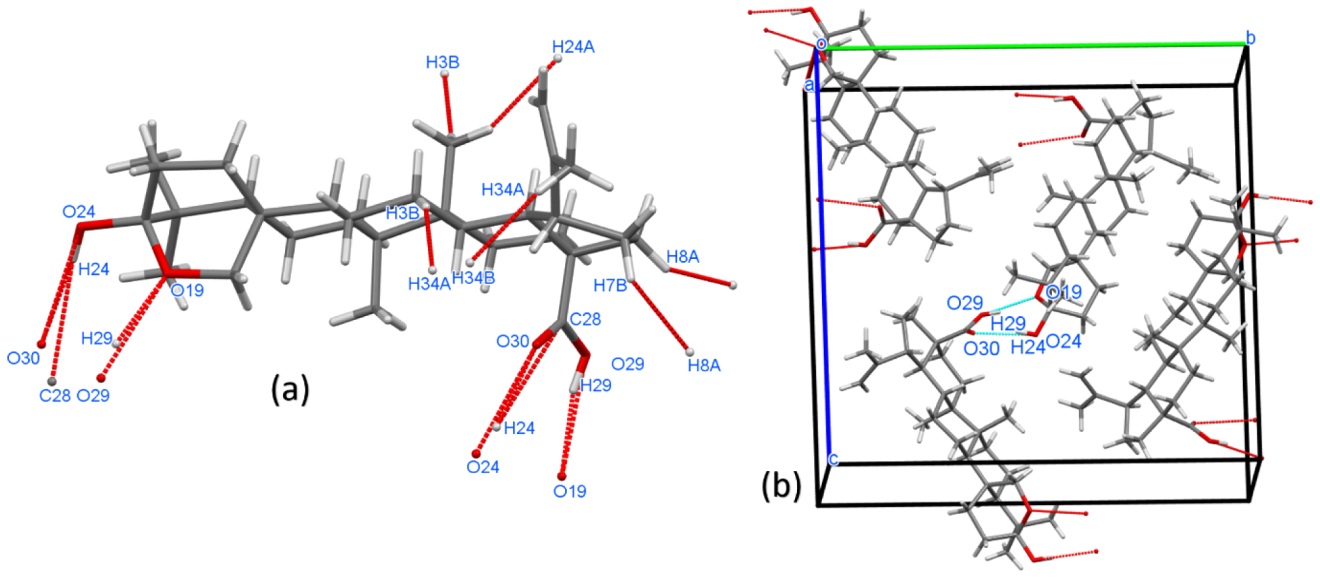

Figure 6. (a) The dominant weak C−H···O hydrogen bonds found in the crystal of 1, (b) molecular packing of the unit cell of compound 1.

Table 2. Comparison of Experimental Bond Lengths (Å), Bond Angles (Deg), and Dihedral Angles (Deg) with Theoretical Values Obtained Using B3LYP/6-311++G (d,p) Level Theory in the Gas Phase for Compound 1

	value (Å)			value (°)			value (°)	
Bond lengths	Expt.	Theor	Bond angles	Expt.	Theor	Dihedral angle	Expt.	Theor.
O19−C18	1.438 (7)	1.436	C18−O19−C14	113.8 (4)	114.1	O24−C18−C17-C16	171.3	167.9
O19−C14	1.449 (7)	1.441	C18−O24−H24	109.5	107.3	O24−C18−O19-C14	179.2	175.7
O24−H24	0.8200	0.964	C28−O29−H29	109.5	106.5	C18−C17−C16-C15	3.01	5.19
O24−C18	1.400 (6)	1.404	C26−C13−C1	111.5 (4)	111.9	C18−O19−C14-C15	8.64	11.83
O30−C28	1.205 (6)	1.207	C26−C13−C12	110.4 (4)	109.9	H24−O24−C18-C17	−170.6	−153.9
O29−H29	0.8200	0.969	C20−C13−C26	107.7 (4)	107.5	C28−C9−C5-C6	75.5	70.6
O29−C28	1.327 (7)	1.362	O19−C18−17	106.6 (5)	107.4	H29−O29−C20-C9	166.9	177.0
C13−C26	1.545 (7)	1.560	O19−C18−C23	109.4 (4)	108.9	C7−C6−C30-C2	106.3	96.6
C23−C25	1.533 (8)	1.544	O24−C18−O19	106.4 (4)	105.8	C7−C6−C30-C24	−72.80	−81.6
C23−C27	1.517 (9)	1.540	O24−C18−C17	106.7 (5)	107.4	C34−C12−C13-C26	174.4	172.0
C5−C6	1.548 (8)	1.549	O24−C18−C23	114.0 (5)	113.2	C14−C15−C1-C13	77.83	82.54
C9−C28	1.517 (8)	1.533	O30−C28−O29	122.2 (6)	120.8	C15−C1−C13-C26	−69.64	−70.36
C22−C23	1.579 (7)	1.581	O30−C28−C9	125.4 (5)	126.1	C6−C5−C9-C8	−37.66	−42.39
C12−C4	1.565 (7)	1.577	O29−C28−C9	112.4 (5)	111.7	C6−C7−C8-C9	−30.62	−27.21
C12−C34	1.541 (7)	1.551	C30−C6−C5	117.3 (5)	117.7	C17−C18−C23-C25	175.68	174.39
C30−C2	1.314 (9)	1.335	C30−C6−H6	108.8	107.8	C17−C18−C23-C27	−65.27	−67.62
C30−C24	1.49 (10)	1.50	C30−C6−C7	109.0 (5)	110.6	C21−C22−C23-C27	−94.59	−94.59
C2−H2A	0.930	1.084	C30−C2−H2B	120	121	C23−C22−C15-C14	49.28	44.85
C13−C12	1.590 (7)	1.611	H2A−C2-H2B	120	118	C5−C6−C30-C24	169.49	169.0

Table 3. Analysis of Weak C−H···O Hydrogen Bonds Stabilizing the Unit Cell

No	D-H···A	D-H [Å]	H···A[Å]	D···A[Å]	<(DHA)	Symmetry Codes
1	O29H29···O19	0.820	1.905	2.712	167.62	1.5-x,1-y,-1/2+z
2	O24H24···O30	0.820	2.017	2.795	158.10	1.5-x,1-y,-1/2+z

molecular surface, these interactions do not significantly affect structural stability (Figure 7d). In contrast, C···C/C···C interactions account for only 1.2% of the contacts (Figure 7e). Figure 7f shows the detailed percentages of various contributions to the Hirshfield surface. Thus, contact analysis of this isolated compound 1 suggests that O−H···O hydrogen bonds drive molecular alignment and crystal packing formation (Figure 6b).

3.4. Antioxidant Activity. The IC_{50} (Inhibition concentration 50) value was then determined using linear regression analysis based on the plot of the scavenging activity (%) or inhibition (%) against log concentration (Figure 8). The IC50 value was calculated to determine the sample concentration required to inhibit 50% radicals. Samples with higher antioxidant activity have lower IC_{50} values. Based on the observed IC_{50} value, isolated compound 1 (ethanolic solution) (13.772 μg/mL) had the highest level of antioxidant activity, followed by standard reference (ascorbic acid) and compound 1 (aqueous solution) (Table 4). The IC_{50} value of compound 1 (ethanolic solution) was lower than that of ascorbic acid

https://doi.org/10.1021/acsomega.4c03406
ACS Omega 2024, 9, 39484−39502

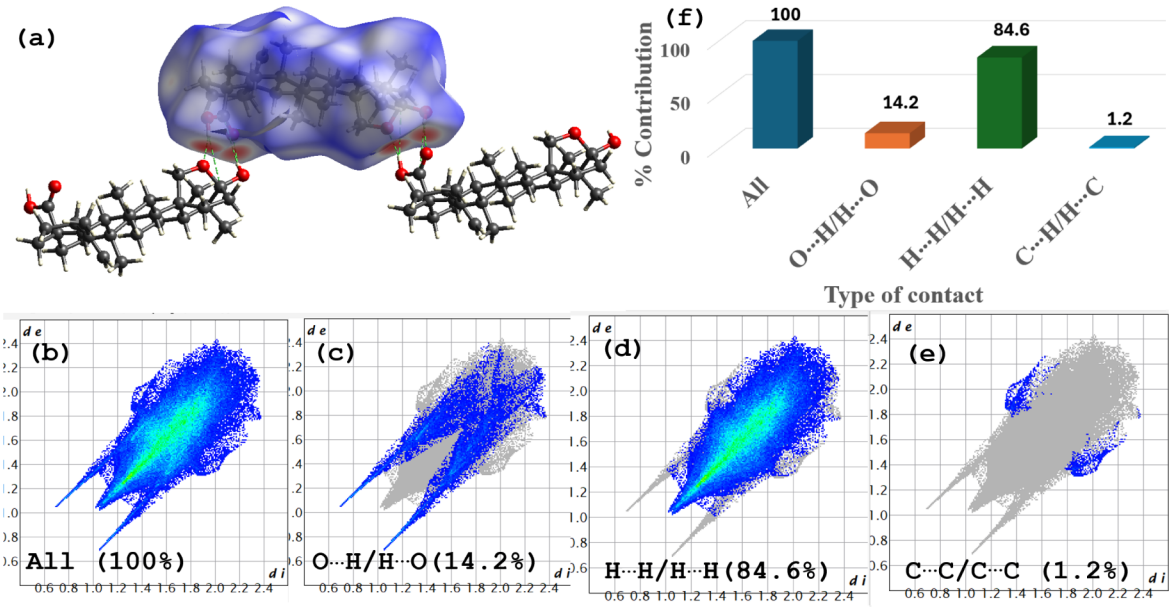

Figure 7. (a) shows the molecular Hirshfeld surface d_{norm}, with red spots highlighting the O−H··· contacts between molecules in compound 1. The Hirshfeld surface plot displays various orientations. (b-e) 2D fingerprint plots depict the contributions of individual interactions, and(f) a bar graph presents the relative contributions of various intermolecular interactions to the Hirshfeld surface area in compound 1.

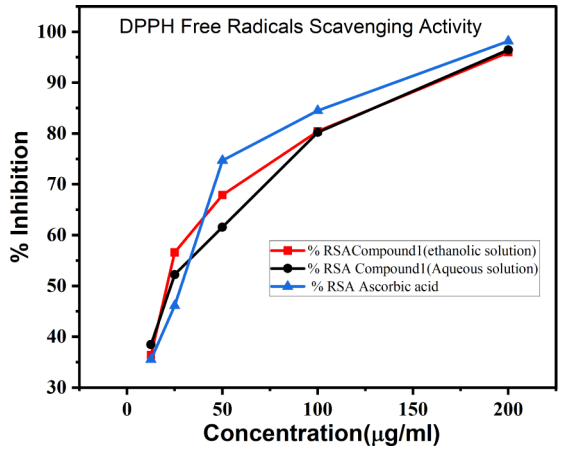

Figure 8. DPPH free radicals scavenging activity of compound **1** in ethanol and aqueous solvent.

(19.712 μg/mL), which is an interesting observation. The compound **1** ethanolic solution exhibits greater antioxidant activity than the compound **1** aqueous solution. The variance in antioxidant activity of compound 1 between ethanol and aqueous solutions may result from differences in solubility and concentration. The high solubility of compound **1** in ethanol alters its interaction with reactive species, potentially affecting the antioxidant activity observed in the DPPH assay. Additionally, variations in concentration due to solubility discrepancies between ethanol and water could contribute to differing activity levels.

Antioxidant activity deemed intermediate has IC_{50} values between 50 and 100 μg/mL. On the other hand, compounds with an IC50 value in the range of 10 to 50 μg/mL are thought to have strong antioxidant activity. Thus, isolated compound **1** has strong antioxidant properties.

3.5. BSA and HSA Binding Studies. Despite being extensively studied, and functionally similar, human serum albumin (HSA) and bovine serum albumin (BSA) exhibit interesting differences. Both are globular transport proteins in the bloodstream, composed of three homologous domains and rich in alpha-helices.[35] However, a subtle difference emerges in their surface hydrophobicity, with HSA being slightly more hydrophobic than BSA. This seemingly minor difference causes significant variations in their bulk behavior and adsorption properties. As a result, despite their structural similarity, HSA and BSA may have different roles in biological processes. This is particularly evident in applications such as drug delivery, cell culture, and protein engineering, where these subtle variations can have a large impact. To investigate the binding behavior of compound **1** with these biomacromolecules, a multipronged approach was employed.[36] UV absorption spectroscopy and fluorescence measurements were used to elucidate the interaction profile of compound **1** with target biomacromolecules. The quenching constant (Ksv), bimolecular quenching constant (Kq), binding constant (Kb), and the number of binding sites (n) were determined by analyzing the obtained

Table 4. Antioxidant Activity of Compound 1 in Various Solvents and Compared to Reference Drug[a]

		Absorbance at 517 nm (%RSA)					
S. No.	Compound	12.5 μg/mL	25 μg/mL	50 μg/mL	100 μg/mL	200 μg/mL	$IC_{50}\mu$g/mL
1.	Compound 1 (ethanolic solution)	36.382	56.595	67.872	80.425	95.957	13.772
2.	Compound 1 (aqueous solution)	38.444	52.222	61.555	80.222	96.444	23.846
2.	Ascorbic Acid	35.510	46.122	74.693	84.489	98.163	19.712

[a]IC_{50} value represents the concentration of three experiments required to exhibit 50% antioxidant activity.

https://doi.org/10.1021/acsomega.4c03406
ACS Omega 2024, 9, 39484−39502

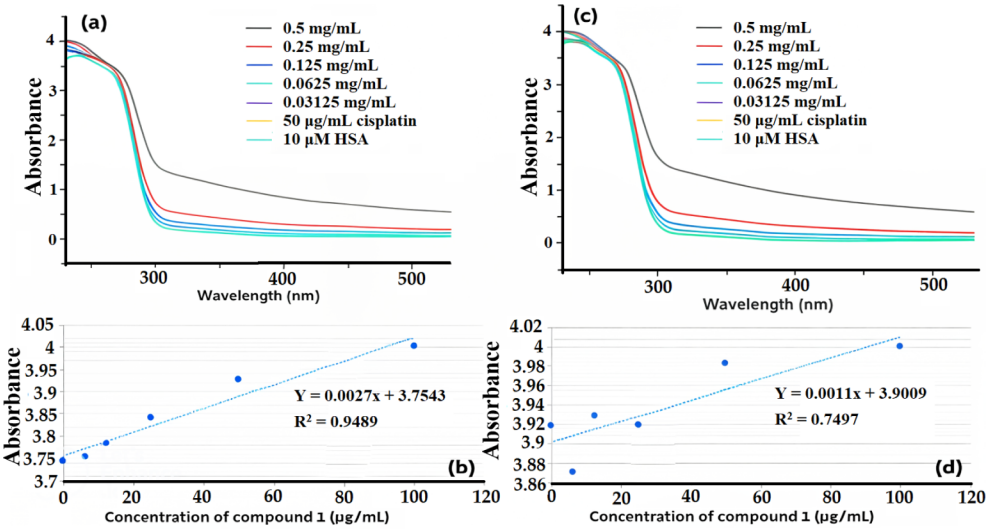

Figure 9. Absorption of HSA treated with different concentrations of compound **1** at (a) 300 K and (c) 310 K. Corresponding regression lines plotted against HSA absorbance for different concentrations of compound **1** at (b) 300 K and (d) 310 K.

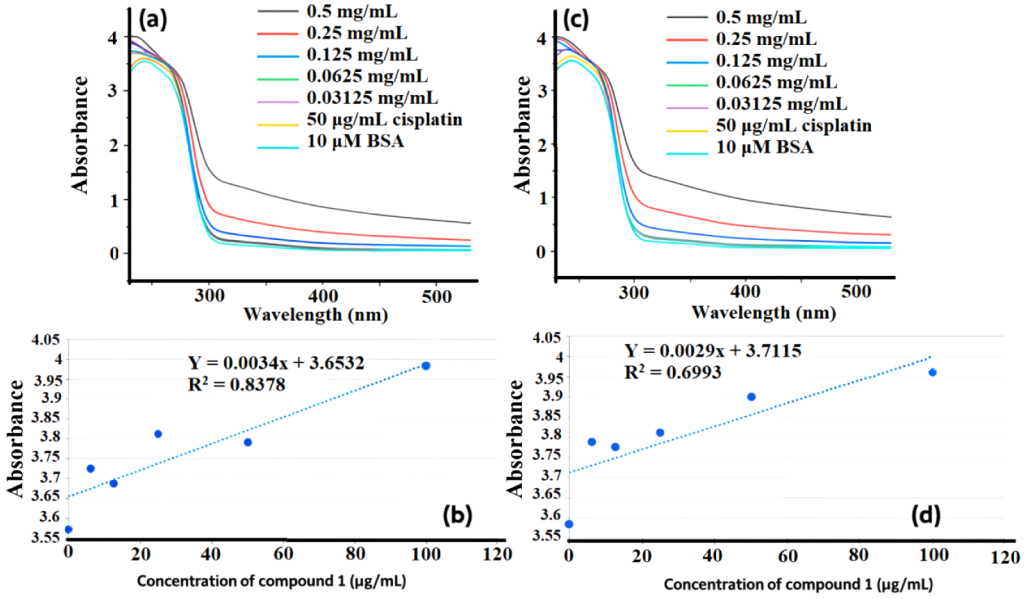

Figure 10. Absorption of BSA treated with different concentrations of compound 1 at (a) 300 K and (c) 310 K. Corresponding regression lines plotted against BSA absorbance for different concentrations of compound 1 at (b) 300 K and (d) 310 K.

findings at two temperatures using the Stern−Volmer (eq 1) and modified Stern−Volmer eq (eq 2).

$$Fo/F = 1 + Ksv[Q] \quad (1)$$

$$\log(F0\text{-}F)/F = \log Kb + n\log[Q] \quad (2)$$

$$kq = Ksv/\tau 0 \quad (3)$$

where F0 and F are the fluorescence intensities in the absence and presence of compound **1** and correspond to fluorescence intensities measured at different quencher concentrations (Q); Kb, Ksv, Kq, n, and $\tau 0$ stand for binding constants, Stern−Volmer constant, quenching rate constant, binding site, and average fluorescence lifetime of HSA and BSA with quencher having a value of 10^{-9} s, respectively.

3.5.1. UV Absorption Spectra Analysis. The interaction of isolated compound **1** with the biomolecular proteins human serum albumin (HSA) and bovine serum albumin (BSA) was analyzed using UV−visible absorption spectroscopy and fluorescence quenching experiments. UV−visible spectroscopic titration of compound 1 with BSA and HSA protein molecules at different temperatures. Figures 9 and 10 show the UV−visible spectral titration of compound **1** with BSA and HSA at different concentrations and temperatures. Corresponding regression lines were plotted for HSA and BSA absorbance at 300 and 310 K for different concentrations of compound 1 (Figures 9 and 10). The concentration of 3β,25-expoxy-3α-hydroxylup-20(29)-en-28-oic acid (compound **1**) was varied, while the concentrations of bovine serum albumin (BSA) and human serum albumin (HSA) were held constant. UV−vis spectra of HSA displayed absorption bands at 221.8 and 268.75 nm at 300 K (BSA showed bands at 266.12 and 239.6 nm at 300 K). At the elevated temperature of 310 K, absorption bands were observed at 244.29 and 272.8 nm (and

https://doi.org/10.1021/acsomega.4c03406
ACS Omega 2024, 9, 39484−39502

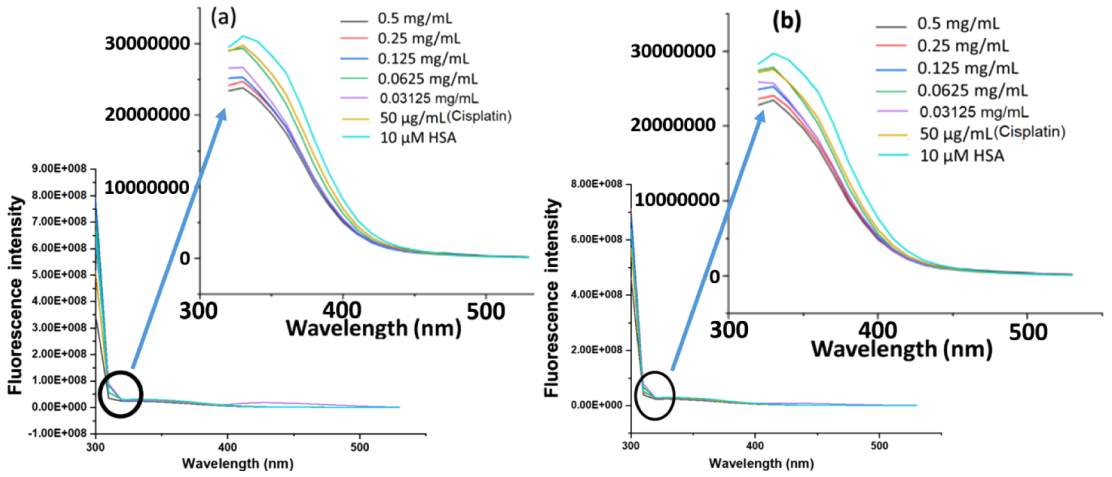

Figure 11. Fluorescence spectra of HSA (fixed at 10 μM) in the presence of various compound concentrations, including a fixed amount of cisplatin (50 μg/mL) at (a) 300 K and (b) 310 K. An enlarged view of the spectra is shown in the inset.

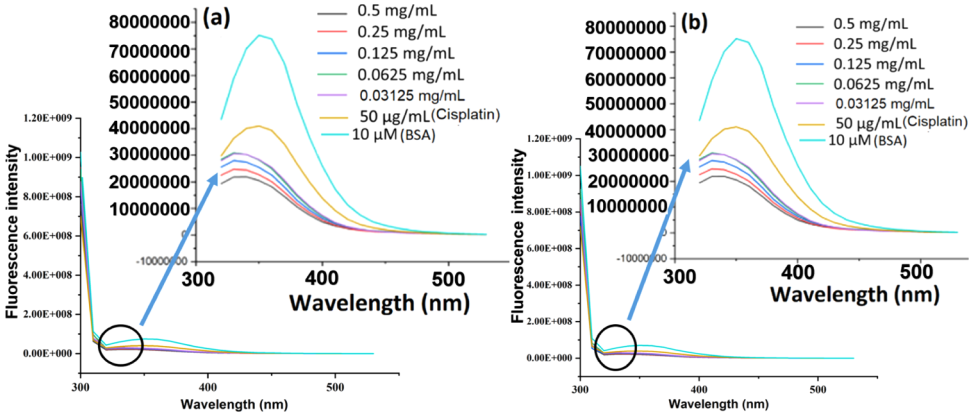

Figure 12. Fluorescence spectra of BSA (fixed at 10 μM) in the presence of various compound concentrations, including a fixed amount of cisplatin (50 μg/mL) at (a) 300 K and (b) 310 K. An enlarged view of the spectra is shown in the inset.

268.2 and 243.5 for BSA). These absorption bands, especially in the range of 268−285 nm are characteristic of the $\pi \rightarrow \pi$ transitions in the aromatic residues tryptophan, tyrosine, and phenylalanine (Figure 9,c). Additionally, another absorption band is attributed to the backbone structure of macromolecules. Upon addition of compound **1** to the protein solution, similar absorption bands appeared, but interestingly, the intensity of these bands increased without a significant shift in wavelength. These results indicate the existence of interactions between compound 1 and biomolecules (BSA and HSA). Figures 9a,c and 10a,c show that the absorption of both HSA and BSA increases with increasing compound **1** concentration after 24 h of incubation at 300 and 310 K. This suggests that compound 1 could interact with macromolecules to form 3β,25-epoxy-3α-hydroxyup-20(29)-N-28-oic acid-macromolecule complexes.

This trend shows that the highest concentration of compound **1** at 0.5 mg/mL produced the maximum absorbance intensity, followed by 0.25 mg/mL, 0.125 mg/mL, and 0.0625 mg/mL, which is consistent with the results observed at 300 K (27 °C) and 310 K (37 °C). consistent. Likewise, according to Figure 10a,c, the absorbance of BSA increased with increasing concentration of compound **1** after incubation at 300 and 310 K. Likewise, the highest concentration of compound 1 at 0.5 mg/mL produced the highest absorbance intensity, followed by 0.25 mg/mL, 0.125 mg/mL, and 0.0625 mg/mL, consistent with the results obtained at 300 and 310 K incubation temperatures. To evaluate the interaction between compound **1** and human and bovine serum albumin (HSA and BSA), the impact of compound concentration on absorbance intensity was examined at two different temperatures: 300 and 310 K. Every protein solution's absorbance was measured after incubation, and regression analysis was performed on the collected data. There was a significant connection (R^2 = 0.9489) between compound **1** concentration and HSA absorbance at 300 K. This suggests that compound **1** and HSA may bind together as there is a dose-dependent rise in absorbance. Likewise, a positive association (R^2 = 0.7497) was noted at 310 K, however, it was not as strong as it was at 300 K (Figure 9b,d).

For BSA, the results followed a similar trend, as shown in Figure 10a−d. There is a positive correlation between absorbance and compound **1** concentration at 300 K (R^2 = 0.8378) and 310 K (R^2 = 0.6993). This again suggests a dose-dependent binding between BSA and compound **1**, with the interaction likely to be stronger at 300 K compared to 310 K.

3.5.2. Fluorescence Measurements Analysis. Fluorescence spectroscopy provides a valuable method for investigating the interactions between potential drugs and human serum albumin (HSA) and bovine serum albumin (BSA). Proteins contain specific residues that play a crucial role in their

https://doi.org/10.1021/acsomega.4c03406
ACS Omega 2024, 9, 39484−39502

Table 5. Quenching Constant (Ksv), Binding Constant (Kb), and Binding Site (n) Were Obtained Using Stern−Volmer and the Modified Stern−Volmer Equation

	At 300 K				At 310 K			
Bio macromolecules	K_{sv}mg/mL	$K_q$mg/mL·s	$K_b$mg/mL	n	K_{sv}mg/mL	$K_q$mg/mL·s	$K_b$mg/mL	n
HSA	0.54	5.41×10^9	1.35	0.95	0.47	4.7×10^9	1.32	0.88
BSA	3.49	3.49×10^9	3.65	0.93	3.27	3.27×10^9	3.51	0.85

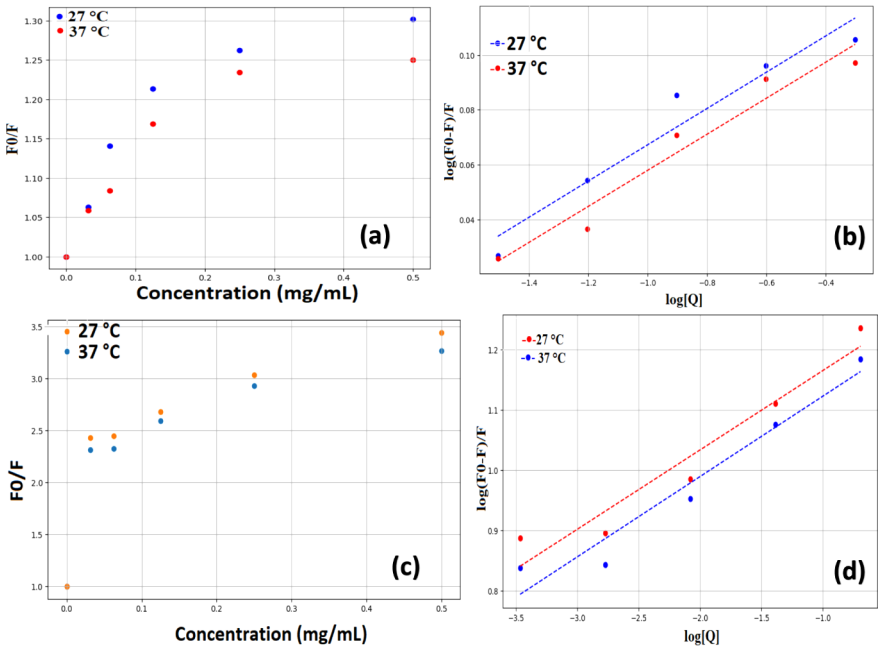

Figure 13. Comparison of Stern−Volmer plots and modified Stern−Volmer plots for HSA and BSA at two temperatures. Plots of F0/F versus concentration [Q] and log (F0 - F)/F versus log [Q] illustrate the quenching effect of compound 1 on HSA (a, b) and BSA (c, d).

fluorescent properties. Certain residues, such as tryptophan, can be extremely responsive to alterations in their immediate surroundings. This high level of sensitivity makes them perfect for monitoring protein conformational changes, denaturation, and binding events with other molecules.

During the examination of HSA, a thorough investigation was conducted to analyze the interaction between compound **1** and HSA using fluorescence spectroscopy. Monitoring the intrinsic fluorescence emissions of HSA (also for BSA) in the spectral range of 300−550 nm, the concentration of compound **1** was incrementally varied, as shown in Figure 11a,b. By setting the concentration of HSA at 1.0×10^{-5} M (or 10 μM), and gradually increasing the concentrations of compound **1** from 0.03125 mg/mL to 0.5 mg/mL, a noticeable reduction in the fluorescence intensity of the protein band was observed. An illustration, shown in Figure 11a,b, highlights this connection at various temperatures. Remarkably, there was a noticeable change in the emission maximum, shifting from 330.0 to 326.0 nm at temperatures of 300 K (27 °C) and 310 K (37 °C) (310.15K). This shift suggests a decrease in the tryptophan fluorescence quantum yield of HSA, likely caused by the influence of compound **1** as well as temperature. Interestingly, at both 300 and 310 K, the concentration of compound **1** did not cause a significant change in the emission maximum shift. However, further examination of the emission shift reveals a minor blue shift. Nevertheless, there were clear changes in fluorescence intensity. In the investigation of BSA, a comparable pattern was noted, with a fixed concentration of 10 μM and varying concentrations of compound 1. At temperatures of 300 and 310 K, the emission maximum shifted from 310.0 to 300.0 nm, as shown in Figure 12a,b.

This shift in fluorescence maximum suggests a decrease in the polarity of the microenvironment, as indicated by the blue shift. The binding interaction of the isolated compound **1** with varied concentrations was also compared with cisplatin as a standard reference against protein fluorescence at a concentration of 0.05 mg/mL (50 μg/mL). Both cisplatin and compound (1) caused a decrease in the fluorescence intensity of BSA. Remarkably, cisplatin demonstrated this effect at a lower concentration than compound **1**. It seems that compound **1** has the potential to mimic the way cisplatin interacts with BSA, although its binding affinity is slightly weaker. When it comes to HSA, cisplatin also showed a notable decrease in fluorescence intensity at a lower concentration. Similarly, compound **1** produced a similar effect on HSA fluorescence, although it required a slightly higher concentration compared to cisplatin. This consistent pattern indicates that compound **1** may similarly interact with HSA to cisplatin, although possibly with a lower binding strength. Some important parameters, such as the Stern−Volmer quenching constant (Ksv), quenching rate constant (Kq), binding constant (Kb), and number of binding sites (n), were calculated to elucidate the mechanism of fluorescence quenching due to binding interactions and the effect of temperature variation on the experiment. These calculations utilized the Stern−Volmer equation ($kq = Ksv/\tau 0$, where $\tau 0$ is typically 10^{-9} s) and the modified Stern−Volmer equation. The resulting parameters are presented in Table 5.

https://doi.org/10.1021/acsomega.4c03406
ACS Omega 2024, 9, 39484−39502

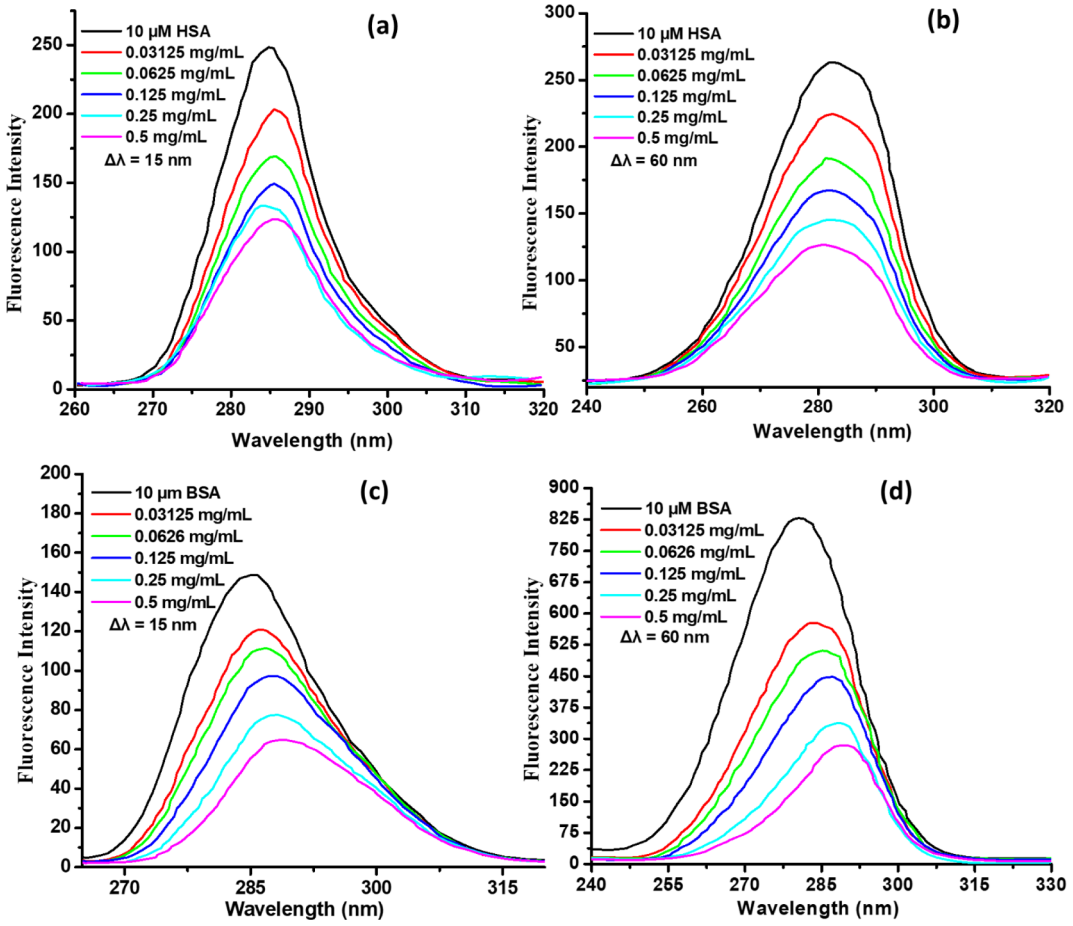

Figure 14. Synchronous fluorescence spectra of HSA and BSA. Shown are spectra at $\Delta\lambda$ = 15 nm (a,c) and $\Delta\lambda$ = 60 nm (b,d) for various concentrations of the compound with a fixed concentration of HSA and BSA.

A significant interaction between the quencher molecule and both HSA and BSA is indicated by the results presented in Table 5. The explanation for this is that the binding constants (Kb) for both biomacromolecules are relatively high, with HSA having a value of 1.35 and BSA having a value of 3.65. In addition, both HSA and BSA have a single binding site (n), indicating that each biomolecule has just one particular binding site for the quencher. The high Kb and n = 1 data align more closely with static quenching. Static quenching involves the formation of a stable complex between the quencher and the biomacromolecule in its ground state, resulting in a decrease in fluorescence emission. Thus, according to the data shown in Table 5 and Figure 13, it is probable that static quenching is the primary mechanism involved. This implies that the quencher forms stable complexes with HSA and BSA, resulting in a reduction in their fluorescence. The experiment revealed interesting temperature dependence. The Ksv values of both HSA and BSA showed a decreasing trend as the temperature increased from 300 to 310 K. This indicates reduced accessibility of the fluorophore (fluorescent molecule) to the quencher molecule. This trend implies that the binding interactions between biomacromolecules (HSA and BSA) and quenchers weaken at higher temperatures. However, the change in Ksv value is relatively small, indicating that the quenching process itself is not significantly affected by temperature changes. Furthermore, the binding constants (Kb) of HSA and BSA showed minimal changes between the two temperatures. This indicates that the binding affinity between the biomacromolecule and the quencher remains relatively constant despite temperature fluctuations from 300 to 310 K). Finally, the number of binding sites (n) remained consistent at approximately 1 at both temperatures. This suggests that only a single type of quencher binding site exists on these biomacromolecules.

The bimolecular quenching constant Kq was calculated according to the following eq 1 based on the quenching constant (Ksv) results obtained from the Stern−Volmer equation.

$$kq = Ksv/\tau 0$$

where τ° is the average protein lifetime in the absence of quencher (typically about 10^{-9} s for biopolymers[37] and Ksv is the Stern−Volmer constant. The Kq values obtained for BSA and HSA are listed in Table 5. To provide clarity, the results were changed from mg/mL to standard units ($M^{-1}s^{-1}$). The Kq values of HSA and BSA at 300 and 310 K are approximately 1.22 × 10^{12} M^{-1} s^{-1}; (300 K), 0.99 × 10^{12} M^{-1} s^{-1}; (310 K), 7.36 × 10^{12} M^{-1} s^{-1}; (300 K), and 6.90 × 10^{12} M^{-1} s^{-1}; (310 K), respectively. Notably, these values are significantly higher than the maximum collision quenching constant (2.0 × 10^10 M^{-1} s^{-1}) of various quenchers with biomolecules.[38] However, the temperature shift from 300 to 310 K resulted in a slight alteration in Kq values, suggesting that temperature influences the HSA-compound binding interaction. Considering that the rate constant of the protein quenching process triggered by compound 1 in this experiment

https://doi.org/10.1021/acsomega.4c03406
ACS Omega 2024, 9, 39484−39502

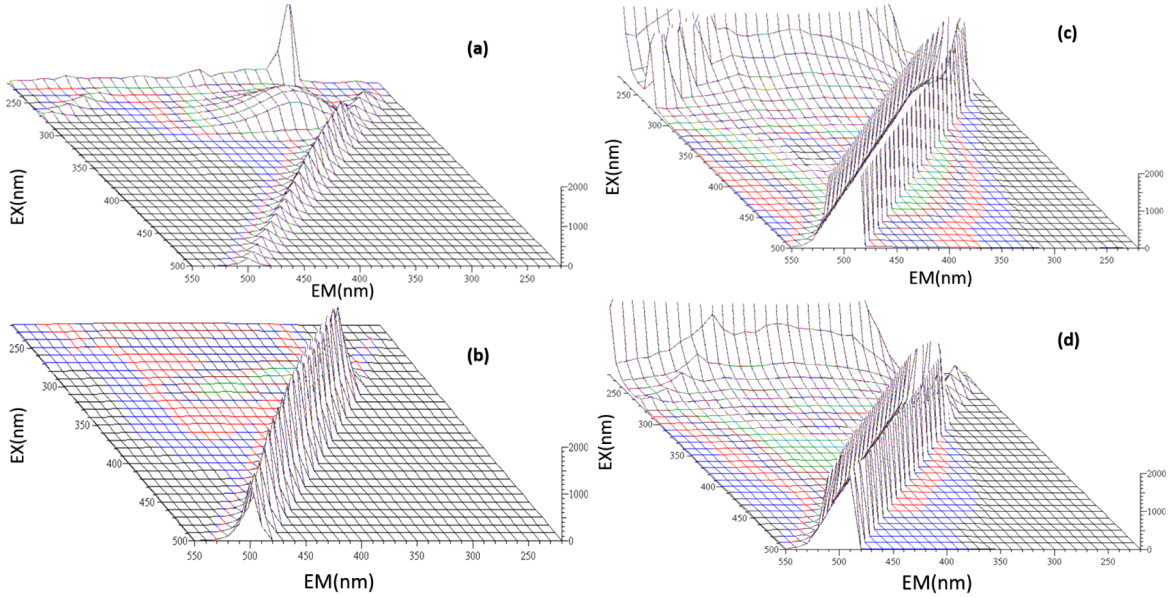

Figure 15. 3D-fluorescence spectra-Excitation−Emission Matrix (EEM) spectra of: (a) HSA (Human Serum Albumin) in its native state. (b) BSA in its native state. (c) HSA after complexation with 0.5 mg/mL (concentration). (b) BSA (Bovine Serum Albumin) after complexation with 0.5 mg/mL (concentration).

is higher than the maximum value of diffusion-limited quenching in solution (~10 × 10 M−1 S−1), it indicates that the interaction between the isolated compound and HSA (or BSA) is mainly static quenching.

3.6. Synchronous Fluorescence and 3D-Dimensional Fluorescence Spectra Analysis. Synchronous fluorescence spectroscopy was employed to investigate the conformational and microenvironmental alterations of serum albumin proteins (HSA and BSA) and the isolated compound **1** (lantabulic acid) during their interaction. The influence of compound **1** on the synchronous fluorescence spectrum of HSA is depicted in Figure 14. At a constant wavelength difference ($\Delta\lambda$) of 15 nm, a minimal shift in the maximum emission wavelength (λ_{max}) was observed, from 284 to 286 nm (Figure 14a). This insignificant change was also observed at $\Delta\lambda$ = 60 nm (Figure 14b), suggesting negligible alterations in the microenvironment surrounding the tyrosine residues of HSA upon binding to compound **1**. Furthermore, a decrease in the fluorescence intensity of HSA was noted with increasing concentrations of compound **1**. Collectively, these observations imply that the interaction between compound **1** and HSA induces a change in the overall fluorophore environment of the protein, although the immediate environment of the tyrosine residues seems relatively unaffected. The more noticeable decrease in fluorescence intensity at $\Delta\lambda$ = 60 nm compared to $\Delta\lambda$ = 15 nm suggests a stronger effect of compound **1** on tryptophan residues in a polar microenvironment.

Synchronous fluorescence spectroscopy revealed conformational changes in BSA upon interaction with compound **1**. This technique isolated the environment near tyrosine ($\Delta\lambda$ = 15 nm) and tryptophan ($\Delta\lambda$ = 60 nm) residues (Figure 14c,d). Red-shifts (6.5 nm for tyrosine, 9.5 nm for tryptophan) and decreased fluorescence intensity were observed for both residues. These results suggest increased polarity around the aromatic residues, possibly due to a shift from a hydrophobic to a more polar environment upon binding to compound **1**. The fluorescence quenching and red-shift implicate both tyrosine and tryptophan residues in the binding process. 3D fluorescence spectroscopy is a powerful tool for studying drug−protein interactions. It can show the way the binding of drug compounds to proteins changes the structure or conformation of proteins. The polarity of the surrounding environment affects the wavelength and intensity of fluorescence. By comparing the emission spectra of the unbound protein (native or BSA) with its drug-bound complex (HSA-compound **1** or BSA-compound **1**), alterations in the protein structure can be detected. Figure 15a,c show the 3D fluorescence spectra of the native state of HSA and BSA, respectively. There are four major peaks in the spectrum shown in Figure 15a. The unique fluorescence of the tryptophan (Trp) and tyrosine (Tyr) residues of the protein is shown by two obvious peaks. According to previously published studies, the polypeptide backbone is the source of another prominent peak. In addition, second-order scattering is represented by the peak at λem = 2λex, while Rayleigh scattering is represented by the peak at λem = λex. Compound **1** interacts with HSA, as illustrated in Figure 15b, resulting in a decrease or attenuation of the peaks, indicating that HSA undergoes microenvironmental and structural changes after binding to compound **1**.

Human serum albumin (HSA) and bovine serum albumin (BSA) have different fluorescence properties because their primary amino acid sequences are different. However, BSA and HSA are only 75.8% identical.[39] Specifically, HSA possesses a unique tryptophan (Trp) residue absent in BSA.[40] Their fluorescence emission spectra reflect this difference.[41] HSA usually shows two clear peaks that are caused by the emissions of its unique tryptophan (Trp) and tyrosine (Tyr) residues (Figure 15a). In contrast, BSA generally exhibits a single broad peak due to the combined fluorescence of its Trp134 and Trp213 residues. In this research, BSA native has a spectrum with a single large peak at 340 nm and a smaller bump at 280 nm. This may be due to tryptophan residues in BSA's intrinsic fluorescence. Proteins commonly contain tryptophan, an aromatic amino acid that exhibits a strong fluorescence signal when excited at around 280 nm. The emission peak around

https://doi.org/10.1021/acsomega.4c03406
ACS Omega 2024, 9, 39484−39502

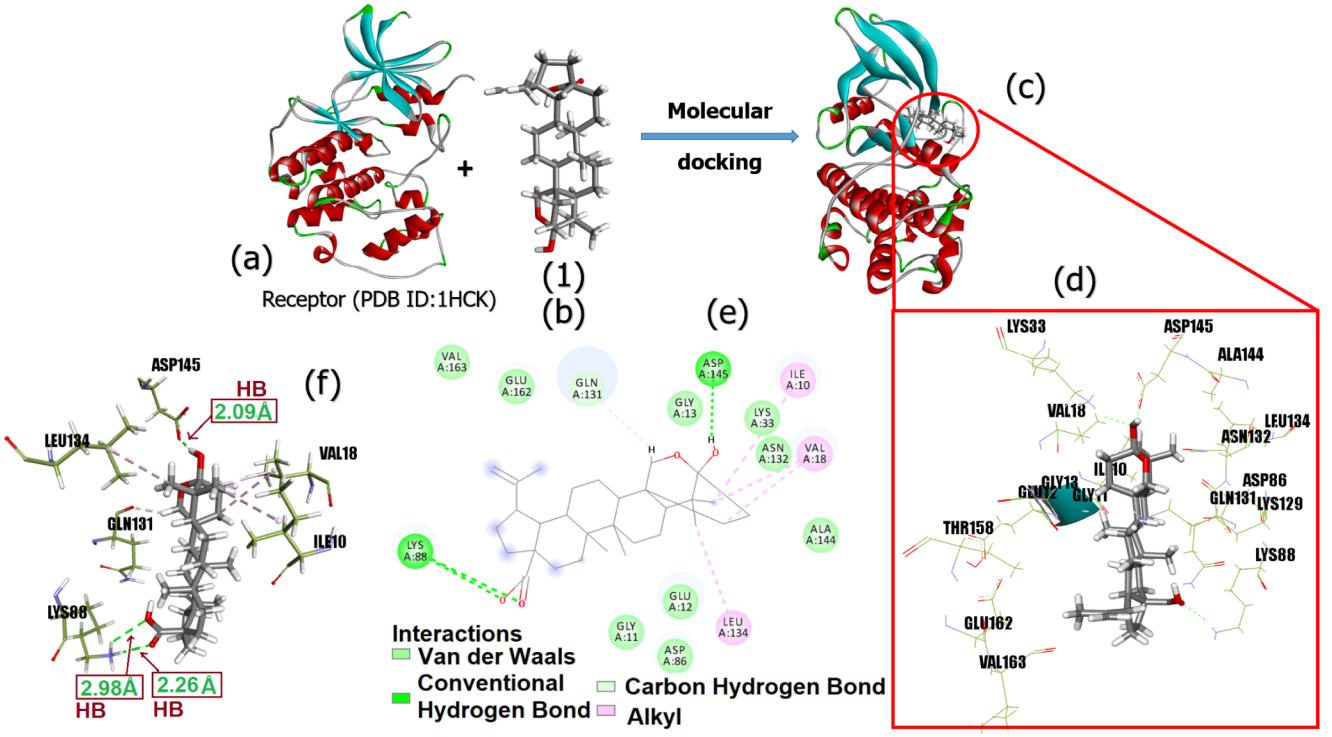

Figure 16. Molecular docking analysis of receptor−ligand interactions: (a) receptor (PDB ID: IHCK), (b) isolated compound **1**, (c) The active site of the receptor with compound **1**, (d) Various interactions between the receptor and compound **1** (e.g., hydrogen bonds, hydrophobic interactions), (e) Delineation of nonbonded interactions (including 2D image of hydrogen bonding (HB)and their distance in image (f), and (f) the interaction of the ligand (compound **1**) with specific amino acid residues of the protein.

340−350 nm is typical for tryptophan fluorescence. The fluorescence intensity of BSA (Figure 15c) was distorted under interaction of the isolated lantabetulic acid. The isolated compound's influencing behavior caused BSA to undergo certain conformational and microenvironmental changes during the interaction (Figure 15d). In brief, 3D fluorescence spectroscopy confirmed the interaction between compound 1 and HSA (or BSA). The peak intensity of HSA (or BSA) either goes down, disappears, or changes shape after the interaction. This shows that the protein's microenvironment and structure have changed. This proves that the interaction worked. However, additional research may be necessary to clarify the precise binding site and the type of interaction, such as hydrophobic or hydrogen bonding.

3.7. Molecular Docking Analysis. Cyclin-dependent kinase 2 (CDK2) plays a crucial role in cell cycle regulation, making it an important target for cancer therapy. Understanding the interaction between potential therapeutic compounds and CDK2 can provide insights into their efficacy and mechanism of action. Therefore, following antioxidant analysis using DPPH, molecular docking with CDK2 was performed to evaluate the binding affinity and interaction mode of the studied compound **1**. Molecular docking is a computer-aided approach to studying the interaction processes of biomolecules. It predicts the binding mode and affinity of possible drug candidates at the active site of the protein. The docking results of the high-resolution crystal structure of human cyclin-dependent kinase 2 (PDB ID: 1hck) showed that the binding pose with a score of −7.2 kcal/mol was the most beneficial (Figure 16a,b). In the kinase 2 active site (Figure 16c), compound **1** interacts with LYS88 and ASP145 residues via hydrogen bonds. These three hydrogen bonds are formed between the carbonyl oxygen and hydroxyl hydrogens of the carboxylic acid group of compound 1 (Figure 16d−e) and the corresponding atoms on the amino acid side chains. Compound 1 is surrounded by many other amino acids, namely GLY11, GLU12, GLY13, LYS33, ASP86, ASN132, ALA144, GLU162, VAL163, GLN131, ILE10, VAL18, and LEU134, leading to van der Waals interactions, and alkyl interactions (see Figure 15f). Based on the 2D image (Figure 16e) and ligand interactions (Figure 16e−f), compound **1** appears to form strong interactions with neighboring amino acid residues mainly through hydrogen bonds. In addition, it establishes van der Waals interactions with amino acid residues in the second layer of the receptor. The compound most likely slowed the system's oxidation process by reacting with the amino acids, resulting in cavities. The compound most likely slowed the system's oxidation process by reacting with the amino acids, resulting in cavities. Compound **1** had significant antioxidant activity, approaching that of ascorbic acid, the reference drug in this study.

3.8. Analysis of Molecular Dynamics Simulations and MM/GBSA Free Energy Calculations for Protein-Compound Complexes. Computational techniques such as molecular dynamics (MD) simulations simulate the physical movements of atoms and molecules over time. In this case, the simulation would focus on interactions between a protein and a small molecule (compound) to understand the way they bind to each other and how their interaction might influence the protein's function.[42]

To assess the stability of the HSA-ligand (Compound-**1**) complex determined from the best docking pose, 100 ns molecular dynamics (MD) simulations were performed at 300 K and atmospheric pressure (Figure 17). Root mean square

https://doi.org/10.1021/acsomega.4c03406
ACS Omega 2024, 9, 39484−39502

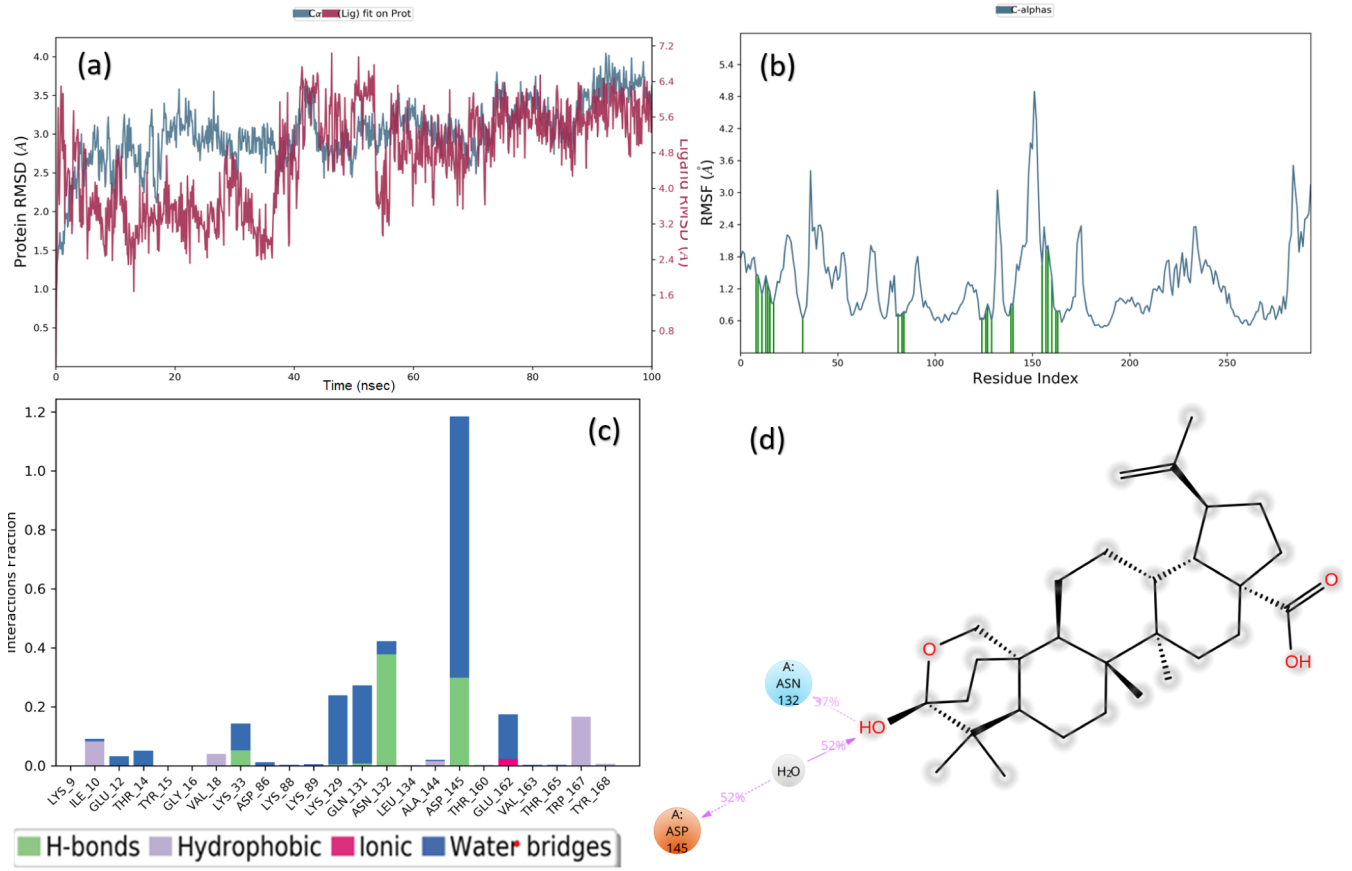

Figure 17. (a) Time-dependent RMSD values during a 100 ns MD simulation for the HSA and ligand-HSA complex, (b) RMSF plot of the ligand-protein complex highlights ligand-binding residues with green vertical lines, and (c and d) Protein−ligand interface illustrates types of ligand interactions with HSA amino acid residues.

deviation (RMSD) analysis provided insights into the overall protein structure and the equilibrium of the simulations. The complex is stable with minimal RMSD fluctuations throughout the simulation, according to the postsimulation trajectory analysis (Figure 17a). This suggests that the ligand effectively attaches and creates enduring hydrogen bonds. During the initial 40 ns of the simulation, there are small variations in the root-mean-square deviation (RMSD) that are within a range of 3 Å from the beginning point. However, these fluctuations can be considered insignificant. The RMSD plot demonstrates that the protein reaches a stable structure (about 3.0 Å) with minor structural changes after 60 to 100 ns. In addition, the ligand RMSD measurement, relative to the protein, verifies the stable placement of the ligand within the binding pocket. Following an initial period of adaptation, the root-mean-square deviation (RMSD) of the ligand becomes stable and remains below 2.5 Å (3.5−1.5 Å from 0 to 100 nms) for the duration of the simulation.

An examination of the RMSF (Root Mean Square Fluctuation) plot was used to assess the amino acids that interacted with the ligand during the simulated period. This plot is displayed in Figure 17b. The green vertical lines in this plot represent the amino acids that are in contact with the ligand and provide important information about the variations of the protein. InFigure 17b, it emphasizes the way the amino acids move around in the protein during the simulation. The 23 amino acids that have been shown to be in interaction with the ligand are indicated by the green vertical lines. The information suggests that the protein's *N*- and C-terminal portions fluctuate more than the middle region does. Variations up to 1.47 Å are seen in the N-terminal residues (9−18), indicating some flexibility. There may be a stable core because the intermediate region (33−145) is more stable and has fewer variations. The C-terminal residues (160−168) fluctuate the most, particularly in the vicinity of VAL163, suggesting a considerable degree of flexibility in this area. This pattern is common to many proteins, where the stable core is less flexible than the terminal portions. These residues fluctuate, with VAL163 showing the largest change of 2.0 Å. Each amino acid in contact with the ligand experiences the following fluctuations in Å: LYS9 (1.47); ILE10 (1.45), GLU12 (1.08); THR14(1.44), TYR15 (1.28); GLY16 (1.15); VAL18 (0.93); LYS33(0.63), ASP86(0.72), LYS88(0.74), LYS89 (0.77), LYS129 (0.65), GLN131(0.78), ASN132 (0.91), LEU134 (0.59), ALA144 (0.92), ASP145 (0.89), THR160 (1.66), GLU162(1.94), VAL163 (2.0), THR165(1.41), TRP167 (0.786), and TYR168 (0.77). Protein−ligand interactions simulated by MD show comparatively stable protein structures with some flexible areas. The protein is flexible during the simulation, as the RMSF data demonstrates. Some residues that come into touch with ligands may be more mobile, but they remain within the acceptable range 2.0 A. The information suggests that the protein's *N*- and C-terminal portions fluctuate more than the middle region does. Variations up to 1.47 Å are seen in the N-terminal residues (9−18), indicating some flexibility. There may be a stable core because the intermediate region (33−145) is more stable and has fewer variations. The C-terminal residues (160−

https://doi.org/10.1021/acsomega.4c03406
ACS Omega 2024, 9, 39484−39502

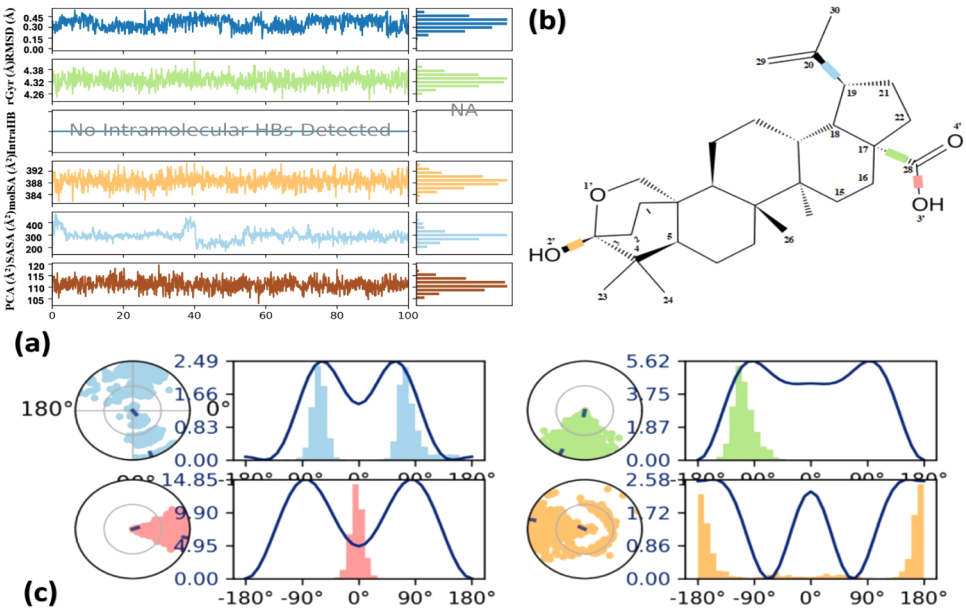

Figure 18. Ligand Properties and Torsion Profile During Simulation (a) This panel shows the properties of the ligand evaluated throughout the 100 ns simulation period, (b to c) The ligand torsion profile for Compound-1 depicts the distribution of scaffold dihedral angles during the simulation. A two-dimensional depiction of the ligand with rotatable, color-coded bonds is shown in the top panel. For every rotatable bond torsion, the dial plots and matching colored bar plots are displayed in the following panels. The torsion angle's conformation is shown visually on dial (or radial) charts during the simulation. The simulation starts at the middle of the radial figure, and time moves outward from there.

168) fluctuate the most, particularly in the vicinity of VAL163, suggesting a considerable degree of flexibility in this area. This pattern is common to many proteins, where the stable core is less flexible than the terminal portions. Figure 17c,d demonstrate the protein−ligand proximity observed during the 100 ns MD simulation. The interactions are categorized into four subtypes: hydrogen bonds, hydrophobic interactions, ionic interactions, and water bridges. Normalization of the stacked bar charts is maintained throughout the trajectory. The adequacy of the specific interaction's maintenance during the 100 ns MD simulation can be determined by analyzing the higher interaction fraction value. Throughout the MD simulations, the receptor made conventional hydrogen connections with GLN131, ASP145, LYS33, and LYS129. ASN132 had the highest interaction fraction among them, just below 0.4, and ASP145 had the lowest, with an interaction fraction slightly above 0.3. LYS33's interaction fraction was roughly 0.05, whereas LYS129 and GLN131's interaction fractions were just slightly significant. A detailed analysis of the interactions and the duration of contact between the amino acids and the ligand is provided. Hydrophobic interactions, including the interaction fraction value, are ILE10 (0.07), VAL18 (0.044), ALA144 (0.033), TRP167 (0.154), and TYR168 (0.015). Water bridges involve ILE10 (03), GLU12 (0.04), THR14 (0.06), LYS33 (0.11), ASP86, LYS88, LYS89, LYS129 (0.24), GLN131 (0.289), ASN132 (0.06), ALA144 (0.0022), ASP145 (0.84), GLU162 (0.13), VAL163 (0.01), and THR165 (0.01). The ionic interaction involves GLU162 (0.03). The results also showed that the average RMSD and rGyr of the ligands are in the range of 0.345−0.36 and 4.34 Å, respectively. The reduction in the fluctuation of rGyr indicates the tightness of the ligand to the protein. The simulation revealed no evidence of intramolecular hydrogen bonds. As shown in Figure 18a, the average solubility of the ligands such as "Molecular Surface Area (MolSA), Solvent Accessible Surface Area (SASA), and Polar Surface Area (PSA) was determined to be 387, 300, and 108 Å.

The analysis of the ligand torsion profile provides valuable information that can be used to determine the pharmacophore properties necessary for interaction with significant residues in proteins. The ligand has four rotatable bonds (RB)−C3−O2′, C17−C28, C19−C20, and C28−O3′—represented by the colors yellow, green, blue, and red in Figure 18b. These colors demonstrate the strong conformational flexibility of the ligand torsion profile. Bonds between atoms C19 and C20 and C3 and O2′ exhibited two distinct conformations with different rotational angles, respectively, while the bond between C28 and O3′ and C17 and C28 atoms exhibits one conformation. separately, with the change in rotation angle on the left and right indicating the probability density of torsion. The potential differences between C19 and C20, C3 and O2′, C28 and O3′ and C17 and C28 are 2.49, 2.58, 14.85, and 5.62 kcal/mol as an units, respectively, indicating a molecular arrangement. The specific properties of the rotatable bonds contribute significantly to the overall binding affinity (Figure 18c). This result indicates the presence of distinct conformations adopted by the compound within the binding pocket of the protein (PDB ID: IHCK).

Molecular dynamics simulations examined ligand interaction dynamics across time. These dynamics were analyzed using binding free energy calculations at 0 and 100 ns. The binding free energy (ΔGbind) dropped from −33.88 kcal/mol at 0 ns to −37.32 at 100 ns. The ligand's binding affinity and stability increase as the system develops to this drop. The following breakdown of energy contributions explains this increase in binding affinity: The electrostatic contribution to the binding energy (ΔGCoulomb) decreased from −10.29 kcal/mol at 0 ns to −12.97 kcal/mol at 100 ns, indicating stronger interactions. The hydrogen bond component (ΔGHbond) decreased more negatively from −0.32 to −1.62 kcal/mol, suggesting increased interaction. Increasing the van der Waals

https://doi.org/10.1021/acsomega.4c03406
ACS Omega 2024, 9, 39484−39502

interaction (ΔGvdW) from −34.19 to −44.27 kcal/mol contributes to the increased binding affinity. The in-depth study of binding energy components and ligand efficiency metrics paints a complicated but complete picture of how the ligand binds. During the simulated time range of 0 to 100 ns, the ligand's binding affinity gets stronger and more stable. This is due to better electrostatic, hydrogen bonding, and van der Waals interactions. Increasing desalination represents a structural change that optimizes these interactions. These trends indicate that the binding is more stable and tighter at 100 ns compared to 0 ns, with stronger specific interactions (Table S2).

4. CONCLUSION

To summarize, the current study reports on extracting and isolating a new lantabetulic acid (**1**) (3*β*,25-expoxy-3*α*-hydroxylup-20(29)-en-28-oic acid) from *R. alata* leaves, in addition to five previously reported compounds. The structure of the isolated compounds was verified using various spectroscopic techniques, including elemental analysis studies, ^{1}Hand ^{13}C NMR, UV, IR, and mass spectroscopy. Compound 1 demonstrates significant antioxidant activity with an IC50 value of 13.772 *μ*g/mL. Notably, the IC50 value of Compound **1** is lower than that of ascorbic acid (19.712 mg/mL). 3*β*,25-expoxy-3*α*-hydroxylup-20(29)-en-28-oic acid **1** was shown to interact with human serum albumin (HSA), and bovine serum albumin (BSA), providing insight into its binding activity. The study also used molecular docking, molecular dynamics simulations and MM/GBSA calculations to prove that the complex is stable and that there is a close interaction at all stages of the simulation, from the beginning to the end. Further studies are needed for validation and potential therapeutic applications, including mechanistic studies as well as in vitro and in vivo studies.

■ ASSOCIATED CONTENT

Data Availability Statement

Data associated with this study has been deposited at the Chemical Crystallographic Data Centre (CCDC) under the accession number 2346661.

Supporting Information

The Supporting Information is available free of charge at https://pubs.acs.org/doi/10.1021/acsomega.4c03406.

Supporting information includes Table S1 (Crystal data and structure refinement), Table S2 (Comparison of Binding Energy Components at 0 and 100 ns MD simulation), Figure S1 (^{1}H NMR spectrum of isolated compound **1**), Figure S2 (^{13}C NMR spectrum of isolated compound **1**), and Figure S3 (Mass spectrum of isolated compound **1**) (PDF)

■ AUTHOR INFORMATION

Corresponding Authors

Mehtab Parveen − *Department of Chemistry, Aligarh Muslim University, Aligarh 202002, India;* orcid.org/0000-0002-0843-9646; Email: mehtab.organic2009@gmail.com

Nurul Huda Abd Kadir − *Faculty of Science and Marine Environment, Universiti Malaysia Terengganu, Kuala Nerus, Terengganu 21030, Malaysia*; Email: nurulhuda@umt.edu.my

Mahboob Alam − *Department of Safety Engineering, Dongguk University, Gyeongju, Gyeongbuk 780714, Republic of Korea;* orcid.org/0000-0002-5188-1130; Email: mahboobchem@gmail.com

Authors

Uzma − *Department of Chemistry, Aligarh Muslim University, Aligarh 202002, India*

Azmat Ali Khan − *Pharmaceutical Biotechnology Laboratory, Department of Pharmaceutical Chemistry, College of Pharmacy, King Saud University, Riyadh 11451, Saudi Arabia;* orcid.org/0000-0001-5955-3783

Shahab A. A. Nami − *Department of Industrial Chemistry, Aligarh Muslim University, Aligarh 202002, India;* orcid.org/0000-0001-9521-0446

Ramesh Kataria − *Department of Chemistry, Panjab University, Chandigarh 160014, India;* orcid.org/0000-0002-4279-4801

Abdul Malik − *Department of Pharmaceutics. College of Pharmacy, King Saud University, Riyadh 11451, Saudi Arabia*

Nurul Afiqah Muhammad Amali − *Faculty of Science and Marine Environment, Universiti Malaysia Terengganu, Kuala Nerus, Terengganu 21030, Malaysia*

Complete contact information is available at: https://pubs.acs.org/10.1021/acsomega.4c03406

Notes

The authors declare no competing financial interest.

■ ACKNOWLEDGMENTS

This work was funded by the Researchers Supporting Project Number (RSP2024R376) at King Saud University, Riyadh 11451, Saudi Arabia.

■ REFERENCES

(1) Petrovska, B. B. Historical review of medicinal plants' usage. *Pharmacogn. Rev.* **2012**, *6* (11), 1−5.

(2) Rout, J.; Sajem, A. L.; Nath, M. Medicinal plants of North Cachar Hills district of Assam used by thetribe. *Indian J. Tradit. Knowl.* **2012**, *11* (3), 520−527.

(3) Saxena, M.; Saxena, J.; Nema, R.; Singh, D.; Gupta, A. Phytochemistry of medicinal plants. *J. Pharmacogn. Phytochem.* **2013**, *1* (6), 168−182.

(4) Roy, M.; Dutta, T. K. Evaluation of phytochemicals and bioactive properties in mangrove associate Suaeda monoica Forssk. ex JF Gmel. of Indian Sundarbans. *Front. Pharmacol.* **2021**, *12*, 584019.

(5) Roy, A.; Datta, S.; Bhatia, K. S.; Jha, B.; Jha, P.; Prasad, R. Role of plant derived bioactive compounds against cancer. *S. Afr. J. Bot.* **2022**, *149*, 1017−1028.

(6) Gurib-Fakim, A. Medicinal plants: Traditions of yesterday and drugs of tomorrow. *Mol. Aspects Med.* **2006**, *27* (1), 1−93.

(7) (a) Rosenoer, V. M.; Oratz, M.; Rothschild, M. A. *Albumin: Structure, function and uses*; Elsevier, 2014. (b) Merlot, A. M.; Kalinowski, D. S.; Richardson, D. R. Unraveling the mysteries of serum albuminâ€"more than just a serum protein. *Front. Physiol.* **2014**, *5*, 299. (c) Matejtschuk, P.; Dash, C.; Gascoigne, E. Production of human albumin solution: A continually developing colloid. *Br. J. Anaesth.* **2000**, *85* (6), 887−895.

(8) Levitt, D. G.; Levitt, M. D. Human serum albumin homeostasis: A new look at the roles of synthesis, catabolism, renal and gastrointestinal excretion, and the clinical value of serum albumin measurements. *Int. J. Gen. Med.* **2016**, *9*, 229−255.

(9) Rayne, S.; Mazza, G. Biological activities of extracts from sumac (Rhus spp.): A review. *Nat. Proc.* **2007**, *62*, 165−175.

(10) Barkley, F. A.; Barkley, E. D. A short history of Rhus to the time of Linnaeus. *Am. Midl. Nat.* **1938**, *19*, 265−333.

(11) Kim, Y.-R.; Kim, G.-C.; Nam, S.-H. Evaluation of the Antifungal Effect of Rhus verniciflua Stokes Extract for Oral Application Potential. *Medicina* **2023**, *59* (9), 1642.
(12) Noro, J. C.; Barrows, L. R.; Gideon, O. G.; Ireland, C. M.; Koch, M.; Matainaho, T.; Piskaut, P.; Pond, C. D.; Bugni, T. S. Tetrahdroxysqualene from Rhus taitensis shows antimycobacterial activity against Mycobacterium tuberculosis. *J. Nat. Prod.* **2008**, *71* (9), 1623−1624.
(13) (a) Lin, P.-C.; Bi, W.-F.; Lin, C.-H.; Lee, F.-P.; Yang, L.-L. Comparing different solvent extracts of Rhus semialata var. roxburghiana stem against ferrous ion-induced lipid peroxidation in mice liver mitochondria. *Nat. Prod. Commun.* **2013**, *8* (5), 621−625. (b) Chew, Y.-L.; Khor, M.-A.; Xu, Z.; Lee, S.-K.; Keng, J.-W.; Sang, S.-H.; Akowuah, G. A.; Goh, K. W.; Liew, K. B.; Ming, L. C. Cassia alata, Coriandrum sativum, Curcuma longa and Azadirachta indica: Food ingredients as complementary and alternative therapies for atopic dermatitis-a comprehensive review. *Molecules* **2022**, *27* (17), 5475.
(14) (a) Parveen, M.; Khan, N. U. Biflavones from the leaves of rhus alata thumb. *Curr. Sci.* **1987**, *56* (22), 1171−1172. (b) Parveen, M.; Khan, N. U.; Achari, B.; Dutta, P. K. Triterpenes from the leaves of rhus alata thumb. *Curr. Sci.* **1989**, *58* (23), 1326−1327. (c) Chiu, C.-L.; Lee, T.-H.; Shao, Y.-Y.; Kuo, Y.-H. Three new triterpenes from the roots of Rhus javanica L. var. roxburghiana. *J. Asian Nat. Prod. Res.* **2008**, *10* (7), 684−688.
(15) Parveena, M.; Basudan, O. A.; Mushfiq, M.; Ghalib, R. M. A new benzofuranic acid from the leaves of Rhus alata. *Nat. Prod. Res.* **2008**, *22* (5), 371−382.
(16) Sheldrick, G. *SADABS: Software for empirical absorption correction*; ScienceOpen Inc., 1996.
(17) Sheldrick, G. J. S. C. SHELXT − Integrated space-group and crystal-structure determination. *Acta Crystallogr., Sect. A: Found. Adv.* **2015**, *71*, 3.
(18) Rigaku, C. *Expert 2.0 r15. Software for data collection and processing*, Schneider Electric, 2011.
(19) Sheldrick, G. Programs for Crystallographic solution and refinement. *Acta Crystallogr. A* **2008**, *64*, 112−122.
(20) Dolomanov, O. V.; Bourhis, L. J.; Gildea, R. J.; Howard, J. A.; Puschmann, H. OLEX2: A complete structure solution, refinement and analysis program. *J. Appl. Crystallogr.* **2009**, *42* (2), 339−341.
(21) Spackman, P. R.; Turner, M. J.; McKinnon, J. J.; Wolff, S. K.; Grimwood, D. J.; Jayatilaka, D.; Spackman, M. A. CrystalExplorer: A program for Hirshfeld surface analysis, visualization and quantitative analysis of molecular crystals. *J. Appl. Crystallogr.* **2021**, *54* (3), 1006−1011.
(22) Hasan, S. R.; Hossain, M. M.; Akter, R.; Jamila, M.; Mazumder, M. E. H.; Rahman, S. DPPH free radical scavenging activity of some Bangladeshi medicinal plants. *J. Med. Plants Res.* **2009**, *3* (11), 875−879.
(23) Braca, A.; Sortino, C.; Politi, M.; Morelli, I.; Mendez, J. Antioxidant activity of flavonoids from Licania licaniaeflora. *J. Ethnopharmacol.* **2002**, *79* (3), 379−381.
(24) Abdel-Tawab, M. Considerations to be taken when carrying out medicinal plant research—what we learn from an insight into the IC50 values, bioavailability and clinical efficacy of exemplary anti-inflammatory herbal components. *Pharmaceuticals* **2021**, *14* (5), 437.
(25) Kochnev, Y.; Hellemann, E.; Cassidy, K. C.; Durrant, J. D. Webina: An open-source library and web app that runs AutoDock Vina entirely in the web browser. *Bioinformatics* **2020**, *36* (16), 4513−4515.
(26) Bowers, K. J.; Chow, E.; Xu, H.; Dror, R. O.; Eastwood, M. P.; Gregersen, B. A.; Klepeis, J. L.; Kolossvary, I.; Moraes, M. A.; Sacerdoti, F. D. Scalable algorithms for molecular dynamics simulations on commodity clusters. *Proceedings of the 2006 ACM/IEEE Conference on Supercomputing*; IEEE, 2006, 84−es.
(27) (a) Kim, K.; Jordan, K. Comparison of density functional and MP2 calculations on the water monomer and dimer. *J. Phys. Chem.* **1994**, *98* (40), 10089−10094. (b) Stephens, P. J.; Devlin, F. J.; Chabalowski, C. F.; Frisch, M. J. Ab initio calculation of vibrational absorption and circular dichroism spectra using density functional force fields. *J. Phys. Chem.* **1994**, *98* (45), 11623−11627. (c) Cramer, C. J. *Essentials of computational chemistry: Theories and models*; John Wiley & Sons, 2013. (d) Becke, A. Density-functional thermochemistry. III. The role of exact exchange. *J. Chem. Phys.* **1993**, *98*, 5648.
(28) (a) Krishnan, R.; Binkley, J. S.; Seeger, R.; Pople, J. A. Self-consistent molecular orbital methods. XX. A basis set for correlated wave functions. *J. Chem. Phys.* **1980**, *72* (1), 650−654. (b) Hariharan, P. C.; Pople, J. A. The influence of polarization functions on molecular orbital hydrogenation energies. *Theor. Chim. Acta* **1973**, *28*, 213−222.
(29) (a) Tomasi, J.; Mennucci, B.; Cammi, R. Quantum mechanical continuum solvation models. *Chem. Rev.* **2005**, *105* (8), 2999−3094. (b) Mennucci, B. Polarizable continuum model. *WIREs Comput. Mol. Sci.* **2012**, *2* (3), 386−404. (c) Herbert, J. M. Dielectric continuum methods for quantum chemistry. *WIREs Comput. Mol. Sci.* **2021**, *11* (4), No. e1519. (d) Barone, V.; Cossi, M. Quantum calculation of molecular energies and energy gradients in solution by a conductor solvent model. *J. Phys. Chem. A* **1998**, *102* (11), 1995−2001.
(30) Frisch, M.; Trucks, G.; Schlegel, H.; Scuseria, G.; Robb, M.; Cheeseman, J.; Scalmani, G.; Barone, V.; Mennucci, B.; Petersson, G. *Gaussian 09, Revision C. 01*. Gaussian Inc., 2009.
(31) (a) Alexander, N.; McDonald, L.; Wesdemiotis, C.; Pang, Y. Native mass spectrometry analysis of conjugated HSA and BSA complexes with various flavonoids. *Analyst* **2024**, *149* (6), 1929−1938. (b) Chatterjee, T.; Pal, A.; Dey, S.; Chatterjee, B. K.; Chakrabarti, P. Interaction of virstatin with human serum albumin: Spectroscopic analysis and molecular modeling. *PLoS One* **2012**, *7* (5), No. e37468.
(32) (a) Bagchi, A.; Sahai, M.; Sinha, S.; Ray, A.; Oshima, Y.; Hikino, H. Semimoronic acid, a new triterpene of Rhus semialata. *J. Chem. Res.* **1985**, No. 12, 398−399. (b) Lee, T. H.; Chiou, J. L.; Lee, C. K.; Kuo, Y. H. Separation and determination of chemical constituents in the roots of Rhus javanica L. var. roxburghiana. *J. Chin. Chem. Soc.* **2005**, *52* (4), 833−841.
(33) Alam, M.; Lee, D.-U. Synthesis, spectroscopic and computational studies of 2-(thiophen-2-yl)-2, 3-dihydro-1H-perimidine: An enzymes inhibition study. *Comput. Biol. Chem.* **2016**, *64*, 185−201.
(34) Spackman, M. A.; McKinnon, J. J. Fingerprinting intermolecular interactions in molecular crystals. *CrystEngcomm* **2002**, *4* (66), 378−392.
(35) Maier, R.; Fries, M. R.; Buchholz, C.; Zhang, F.; Schreiber, F. Human versus bovine serum albumin: A subtle difference in hydrophobicity leads to large differences in bulk and interface behavior. *Cryst. Growth Des.* **2021**, *21* (9), 5451−5459.
(36) Zatón, A. M. L.; Villamor, J. P. Study of heterocycle rings binding to human serum albumin. *Chem.-Biol. Interact.* **2000**, *124* (1), 1−11.
(37) Yu, S.; Perálvarez-Marín, A.; Minelli, C.; Faraudo, J.; Roig, A.; Laromaine, A. Albumin-coated SPIONs: An experimental and theoretical evaluation of protein conformation, binding affinity and competition with serum proteins. *Nanoscale* **2016**, *8* (30), 14393−14405.
(38) Ahmad, F.; Zhou, Y.; Ling, Z.; Xiang, Q.; Zhou, X. Systematic elucidation of interactive unfolding and corona formation of bovine serum albumin with cobalt ferrite nanoparticles. *RSC Adv.* **2016**, *6* (42), 35719−35730.
(39) Bujacz, A. Structures of bovine, equine and leporine serum albumin. *Acta Crystallogr., Sect. D: Biol. Crystallogr.* **2012**, *68* (10), 1278−1289.
(40) Raut, S.; Chib, R.; Butler, S.; Borejdo, J.; Gryczynski, Z.; Gryczynski, I. Evidence of energy transfer from tryptophan to BSA/HSA protected gold nanoclusters. *Methods Appl. Fluoresc.* **2014**, *2* (3), 035004.
(41) (a) Parveen, M.; Aslam, A.; Alam, M.; Siddiqui, M. F.; Bano, B.; Azaz, S.; Silva, M. R.; Silva, P. P. Synthesisand Characterization of Benzothiophene-3-carbonitrile Derivative and Its Interactions with Human Serum Albumin (HSA). *ChemistrySelect* **2019**, *4* (41), 11979−11986. (b) Liu, B.; Lv, T.; Zhao, X.; Zhou, M.; Song, C.; Zeng, C.; Qin, T.; Xu, Z. Fluorescence discrimination of HSA from

https://doi.org/10.1021/acsomega.4c03406
ACS Omega 2024, 9, 39484−39502

BSA: A close look at the albumin-induced restricted intramolecular rotation of flavonoid probe. *Spectrochim. Acta, Part A* **2022**, *264*, 120306. (c) Wang, P.-Y.; Yang, C.-T.; Chu, L.-K. Differentiating the protein dynamics using fluorescence evolution of tryptophan residue (s): A comparative study of bovine and human serum albumins upon temperature jump. *Chem. Phys. Lett.* **2021**, *781*, 138998.

(42) Mahesha; Sapnakumari, M.; Sapnakumari, M.; Chethan, B. S.; Jinkle, T.; Deepa Urs, M. V.; Lingegowda, N.; Lokanath, N. K.; Naveen, S. Multicomponent synthesis, structural and molecular dynamics simulation studies of a novel spirooxindole derivative. *Chem. Phys. Impact* **2024**, *8*, 100467.

https://doi.org/10.1021/acsomega.4c03406
ACS Omega 2024, 9, 39484−39502